Inactivation of BK Channels Mediated by the NH_2 Terminus of the β3b Auxiliary Subunit Involves a Two-Step Mechanism: Possible Separation of Binding and Blockade✪

CHRISTOPHER J. LINGLE,*‡ XU-HUI ZENG,* J.-P. DING,* and XIAO-MING XIA*

From the *Department of Anesthesiology and ‡Department of Anatomy and Neurobiology, Washington University School of Medicine, St. Louis, Missouri 63110

ABSTRACT A family of auxiliary β subunits coassemble with *Slo* α subunit to form Ca^{2+}-regulated, voltage-activated BK-type K^+ channels. The β subunits play an important role in regulating the functional properties of the resulting channel protein, including apparent Ca^{2+} dependence and inactivation. The β3b auxiliary subunit, when coexpressed with the *Slo* α subunit, results in a particularly rapid (~1 ms), but incomplete inactivation, mediated by the cytosolic NH_2 terminus of the β3b subunit (Xia et al., 2000). Here, we evaluate whether a simple block of the open channel by the NH_2-terminal domain accounts for the inactivation mechanism. Analysis of the onset of block, recovery from block, time-dependent changes in the shape of instantaneous current-voltage curves, and properties of deactivation tails suggest that a simple, one step blocking reaction is insufficient to explain the observed currents. Rather, blockade can be largely accounted for by a two-step blocking mechanism ($C_n \rightleftharpoons O_n \rightleftharpoons O^*_n \rightleftharpoons I_n$) in which preblocked open states (O^*_n) precede blocked states (I_n). The transitions between O* and I are exceedingly rapid accounting for an almost instantaneous block or unblock of open channels observed with changes in potential. However, the macroscopic current relaxations are determined primarily by slower transitions between O and O*. We propose that the O to O* transition corresponds to binding of the NH_2-terminal inactivation domain to a receptor site. Blockade of current subsequently reflects either additional movement of the NH_2-terminal domain into a position that hinders ion permeation or a gating transition to a closed state induced by binding of the NH_2 terminus.

KEY WORDS: channel block • K^+ channels • gating mechanisms • Ca^{2+}- and voltage-gated K^+ channels • mSlo channels •

INTRODUCTION

Following perturbations that favor activation of an ion channel, a number of ion channels inactivate: specifically, ion channel open probability diminishes despite the continued imposition of conditions that would normally maintain the channels in open states. For many voltage-dependent K^+ channels including the *Shaker*B channel, an important type of inactivation, often termed ball-and-chain inactivation (Bezanilla and Armstrong, 1977; Hoshi et al., 1990), is thought to result from the movement of an NH_2-terminal peptide domain into a position that physically occludes the mouth of the ion permeation pathway. For inactivation of the *Shaker*B K^+ channel, several lines of evidence support the view that the association of the NH_2-terminal domain with its binding site directly results in blockade of the ion channel. First, the kinetic features of block can be described by a simple, one-step blocking reaction in which binding of the inactivation domain and block are identical. Second, cytosolic channel blockers can impede *Shaker*B K^+ channel inactivation, suggesting the native inactivation domain and cytosolic blockers share portions of a common binding site at the mouth of the ion permeation pathway (Choi et al., 1991; Demo and Yellen, 1991). Third, blockade by untethered NH_2-terminal peptides of the *Shaker*B K^+ channel exhibits features consistent with a simple first-order blocking reaction in which association of the peptide directly results in inhibition of ion permeation (Murrell-Lagnado and Aldrich, 1993a,b).

Ca^{2+}-regulated, voltage-activated BK-type K^+ channels can also exhibit a somewhat similar type of inactivation (Solaro and Lingle, 1992; Solaro et al., 1997; Ding et al., 1998), mediated by the NH_2-terminal domains of either of two auxiliary β subunits, the β2 (Wallner et al., 1999; Xia et al., 1999) or the β3b (Uebele et al., 2000; Xia et al., 2000). Although the inactivation of large conductance Ca^{2+}-regulated, voltage-

---

✪The online version of this article contains supplemental material.

Address for correspondence to Chris Lingle, Department of Anesthesiology, Washington University School of Medicine, Box 8054 St. Louis, MO 63110. Fax: (314) 362-8571; E-mail: clingle@morpheus.wustl.edu activated K^+ channels (BK),[1] like *Shaker* K^+ channel inactivation, is mediated by NH_2-terminal domains, several aspects of the inactivation of BK channels in chromaffin cells and of channels containing the cloned β2 subunit differ from the simple picture of ball-and-chain inactivation proposed for voltage-dependent K^+ channels. In particular, cytosolic blockers of BK channels fail to slow the onset of inactivation, suggesting that such blockers do not impede the movement of the inactivation domain to its blocking site (Solaro et al., 1997; Xia et al., 1999). Furthermore, channel reopening does not occur during the recovery process, which is indicative that the conformational change associated with channel closing can occur independent of the recovery from inactivation (Solaro et al., 1997). Thus, inactivation mediated by the β2 subunit may involve a site that is not homologous to that involved in *Shaker*B K^+ channel inactivation, and perhaps may involve a mechanism of inactivation somewhat different from that described for *Shaker* K^+ channels.

To provide further insight into the mechanisms of BK channel inactivation, here we have examined the properties of inactivation mediated by the β3b subunit in more detail. In contrast to inactivation mediated by the β2 subunit (Wallner et al., 1999; Xia et al., 1999), inactivation produced by the β3b subunit exhibits a much faster, although incomplete, inactivation (Uebele et al., 2000; Xia et al., 2000). The β3b subunit is one of at least four splice variants of the β3 subunit (Uebele et al., 2000). Like the β2 subunit, inactivation mediated by the β3b subunit is not inhibited by occupancy of the BK channel by cytosolic channel blockers (Xia et al., 2000), leaving open the possibility that despite the kinetic differences, the underlying target of the inactivation domain for each subunit might be similar. Here we ask, to what extent does a simple pore-blocking model account for inactivation mediated by the β3b subunit? Taking advantage of the unique kinetic characteristics of inactivation conferred by the β3b subunit, we show that inactivation requires a minimum of two kinetic steps, one of which must be a conducting, but preinactivated state. One physical conception of the two-step mechanism is that the binding step for the association of the NH_2-terminal inactivation domain may be separated from the blocking step itself.

MATERIALS AND METHODS

Expression Constructs

The preparation of all constructs used in this work has been described previously (Xia et al., 2000). The *Xenopus* oocyte expression vector pBF was used to subclone all the DNA constructs (Xia et al., 1998). Constructs in which the COOH and NH_2 termini were removed, previously termed β3b-D3 (COOH terminus–deleted) and β3b-D4 (NH_2 terminus–deleted), are here called β3b-ΔC and β3b-ΔN, respectively.

Expression in Xenopus Oocytes

Methods of expression in *Xenopus* oocytes were as described previously (Xia et al., 1999). SP6 RNA polymerase was used to synthesize cRNA for oocyte injection after DNA was linearized with MluI (Xia et al., 1998). 10–50 nl of cRNA (10–20 ng/μl) was injected into stage IV *Xenopus* oocytes harvested 1 d before. To ensure a molar excess of β subunits to *Slo* α subunits, we usually injected α/β at 1:1 or 1:2 ratios by weight, although, in some cases, ratios up to 1:5 were also examined.

After injection, oocytes were maintained at 17°C in ND96 (96 mM NaCl, 2.0 mM KCl, 1.8 mM $CaCl_2$, 1.0 mM $MgCl_2$, and 5.0 mM HEPES, pH 7.5) supplemented with 2.5 mM sodium pyruvate, 100 U/ml penicillin, 100 mg/ml streptomycin, and 50 mg/ml gentamicin. Oocytes were used 1–7 d after injection of cRNA.

Electrophysiology

All currents were recorded in inside-out patches (Hamill et al., 1981). Currents were typically digitized at 10–50 kHz, although, in some cases, 100-kHz sampling frequencies were used. Currents were filtered at 5–50 kHz (Bessel low-pass filter; −3 dB) during digitization.

During seal formation, oocytes were bathed in ND-96. After excision, patches were quickly moved into a flowing 0 Ca^{2+} solution (contaminant Ca^{2+}plus 5mM EGTA). For inside-out recordings, the pipet extracellular solution was 140 mM potassium methanesulfonate, 20 mM KOH, 10 mM HEPES, and 2 mM $MgCl_2$, pH 7.0. Test solutions bathing the cytoplasmic face of the patch membrane contained 140 mM potassium methanesulfonate (MES), 20 mM KOH, 10 mM HEPES, pH 7.0, and one of the following: 5 mM EGTA (for nominally 0-Ca^{2+}, 0.5-μM, and 1-μM Ca^{2+} solutions), 5 mM HEDTA (for 4- and 10-μM Ca^{2+} solutions), or no added Ca^{2+} buffer (for 60 μM, 100 μM, 300 μM, and 5 mM Ca^{2+} solutions). The procedures for calibration of Ca^{2+} solutions have been described previously (Xia et al., 1999, 2000). Briefly, for a given Ca^{2+}-sensitive electrode, a commercial set of Ca^{2+} standards (WPI) was used to define a calibration curve. Ca^{2+} concentrations of the methanesulfonate-based solutions were determined based on this calibration curve. The values obtained from the commercial set of Ca^{2+} standards were identical to a set of chloride-based Ca^{2+} solutions prepared in this lab in which free Ca^{2+} was defined by a computer program (EGTAETC, obtained from E. McCleskey, Vollum Institute, Portland, OR) using published stability constants. Local perfusion of membrane patches was as described previously (Solaro and Lingle, 1992; Solaro et al., 1997).

Voltage commands and acquisition of currents was accomplished with pClamp7.0 or pClamp8.0 for Windows (Axon Instruments). Current values were measured using ClampFit (Axon Instruments), converted to conductances, and then fit with a custom nonlinear least squares fitting program. Conductances were determined in three ways: from tail currents, from the peak current at a given activation potential, and from steady-state current at a given activation potential. Single conductance-voltage (G-V) curves for activation were fit with a Boltzmann equation with the form:

$$G(V) = G_{max}/(1+(\exp(-V+V_{0.5}))/k) \tag{1}$$

where $V_{0.5}$ is the voltage of half-maximal activation of conductance, and k is the voltage dependence of the activation process (mV). G-V curves for a single patch over a range of Ca^{2+} concentrations were also fit with a set of equations based on a Monod-

---

[1] *Abbreviations used in this paper*: BK, large conductance Ca^{2+}-regulated, voltage-activated K^+ channel; BPTI, bovine pancreatic trypsin inhibitor; DTX, dendrotoxin; MWC, Monod-Wyman-Changeaux.

Wyman-Changeau (MWC) model of activation (see Eq. 5 in Cox et al., 1997):

$$G(V,Ca^{2+}) = (G_{max}/(1 + BL(0)e^{-QFV/RT})), \qquad (2)$$

where L(0) represents the open-to-closed equilibrium at 0 mV in the absence of Ca^{2+} and $B = ((1 + [Ca^{2+}]/K_c)/(1 + [Ca^{2+}]/K_o))^4$, with K_c and K_o the dissociation constants of Ca^{2+} for the closed and open channels, respectively, and Q is the net charge associated with movement from closed to open states. As described in RESULTS, inclusion of blocking transitions from open states allows expansion of Eq. 2 to allow prediction of both tail current and steady-state G-V curves. For all cases in which tail and steady-state G-V curves were fit to a particular model, all curves were fit simultaneously.

In some experiments with Ca^{2+} of 10 μM or less, the online P/N leakage subtraction capability of the Clampex software was used to remove linear components of leak and poorly compensated capacitative currents. When Ca^{2+} exceeded 10 μM, no leakage subtraction procedure was used, since appreciable current could be activated at potentials normally used to define linear components.

Experiments were done at room temperature (21–24°C). All salts and chemicals were obtained from Sigma-Aldrich. 18C6TA was the gift of J. Neyton (Centre National de la Recherche Scientifique, Paris, France).

Model Simulations

Simulation of steady-state expectations for various kinetic schemes were done using Mathcad 8.0 (Mathsoft). Predictions for the kinetic behavior of currents were done using a custom program written in Fortran running under an AIX operating system, using Q-matrix manipulation algorithms from Numerical Recipes (Press et al., 1989). The program allowed evaluation of Markovian models containing up to 30 states, with transition rates between any pair of states being defined by $k(V) = [C] \cdot k(0) \cdot \exp(AV)$, where $A = z/25.26$. [C] corresponds to an optional scaling term for Ca^{2+} concentration (C =1, when the rate is Ca^{2+} independent), and k(0) is the zero voltage rate constant for the transition. The program allows prediction of current waveforms in accordance with protocols similar to those defined by pClamp parameter files.

Online Supplemental Material

Further consideration of the ability of Scheme 2 to account for unusual features of the α + β3b currents is provided online at http://www.jgp.org/cgi/content/full/117/6/583/DC1. This includes all of the following: a comparison of the properties of the Ca^{2+}- and voltage dependence of conductance-voltage curves based on Scheme 1 and Scheme 2 (Figure S1); an examination of expectations for current activation (Figure S2) and deactivation (Figure S3); and a demonstration that Scheme 2 provides an unusual possible explanation for the failure of fast cytosolic channel blockers to compete with the inactivation process (Figure S4).

RESULTS

Two Models for Inactivation

This paper has two primary aims. The first aim is to provide a detailed description of the behavior of currents arising from coexpression of the β3b subunit with *Slo* α subunits. The second aim is to present a kinetic model that appears to account for many of the novel aspects of the observed currents. To help guide the presentation and evaluation of the results, it is useful to introduce here the two primary blocking models that will be considered.

Typically, inactivation of a variety of ion channels, including the *Shaker* type voltage-dependent K^+ channels (Hoshi et al., 1990; Choi et al., 1991; Demo and Yellen, 1991), can be modeled by a simple open channel block scheme given as follows.

$$C_n \underset{k_c}{\overset{k_o}{\rightleftharpoons}} O_n \underset{k_u}{\overset{k_b}{\rightleftharpoons}} I_n$$

(SCHEME 1)

The hallmark of this model is that binding of an inactivation domain to its binding site directly produces functional blockade. Molecules that block the binding of the inactivation domain to its blocking site compete with the inactivation mechanism, resulting in the slowing of inactivation. Furthermore, occupancy of the blocking site by the inactivation domain prevents the direct return of inactivated channels to closed states, therefore, resulting in channel unblocking and reopening during recovery from inactivation. For the case in which n = 5, Scheme 1 corresponds to the voltage-dependent MWC model considered by Cox et al. (1997), with the addition of the blocking reaction from the open states.

We also consider a second type of blocking scheme, which postulates a set of preinactivated, open states (O^*_n) that precede entry into inactivated states (I_n):

$$C_n \underset{k_c}{\overset{k_o}{\rightleftharpoons}} O_n \underset{k_r}{\overset{k_f}{\rightleftharpoons}} O^*_n \underset{k_u}{\overset{k_b}{\rightleftharpoons}} I_n$$

(SCHEME 2)

One physical picture of this model would be that binding of an inactivation domain to a site on the channel precedes a subsequent transition to the inactivated state. The primary mechanistic distinction between Schemes 1 and 2 is that, in the latter, binding of the inactivation domain to its binding site is distinct from the transition that produces inactivation. However, alternative conceptions of the two steps in Scheme 2 are also possible.

How do these two categories of models differ in terms of the characteristics of the currents they predict? From macroscopic currents, Scheme 2 might be expected to differ from Scheme 1 in three primary

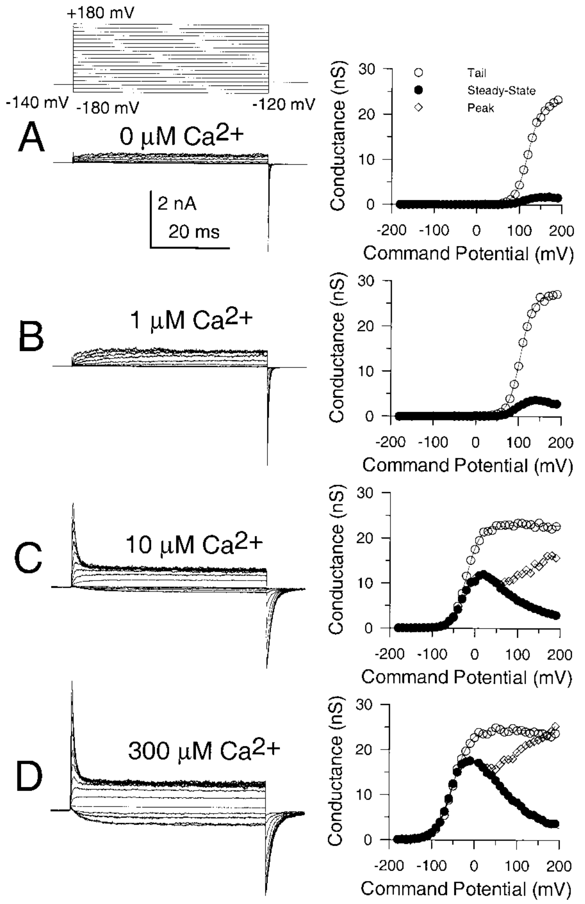

FIGURE 1. Ca^{2+} and voltage-dependent of activation of currents resulting from α + β3b coexpression. In A–D, each set of traces shows currents obtained from an inside-out patch from a *Xenopus* oocyte in which cRNAs encoding human β3b and mouse *Slo* α subunits were coinjected. Channels were activated by the indicated voltage-protocol with (from top to bottom) 0, 1, 10, and 300 μM Ca^{2+}. Panels on the right show conductance measured from peak (◇), steady-state (●), or tail currents (○; measured at 110 μs after the onset of the repolarizing voltage step). In all cases, maximal tail current at −120 mV greatly exceeds the steady-state level of current at +180 mV, indicative of a very rapid unblocking of channels. Also note the similarity in maximal tail current amplitude over all Ca^{2+}. Fitted values of Eq. 1 to the tail current G-V curves were as follows: for 0 μM, $V_{0.5}$ = 120.8 mV and k = 15.22 mV; for 1 μM Ca^{2+}, $V_{0.5}$ = 104.6 mV and k = 14.32 mV; for 10 μM Ca^{2+}, $V_{0.5}$ = −19.6 mV and k = 15.75 mV; and for 300 μM Ca^{2+}, $V_{0.5}$ = −49.2 mV and k = 18.50 mV.

ways. First, dependent on the relative rates of various transitions, channels behaving in accordance with Scheme 2 might show some unusual features in the tail currents after repolarization from inactivating potentials. This might be apparent either as a rising phase in the tail current itself or as a slowing in the time constant of deactivation. Second, Scheme 2 predicts additional complexity in the recovery from inactivation than would be predicted by Scheme 1. Third, Scheme 2 predicts that, at different times during a tail current, channels should be occupying different types of open states. Experiments below test these various possibilities and show that Scheme 2 provides a better explanation for α + β3b currents than Scheme 1.

Rapidly Inactivating Currents Mediated by the β3b Subunit

Message for the β3b subunit was coexpressed with *Slo* α subunits in *Xenopus* oocytes. Currents obtained from inside-out patches expressing α + β3b subunits were both voltage- and Ca^{2+} dependent with activation shifted to more negative potentials as cytosolic Ca^{2+} was increased. The general properties of the currents arising from coexpression of β3b with α subunits have been presented elsewhere (Xia et al., 2000). Briefly, at strong depolarizations and higher Ca^{2+}, α + β3b currents exhibit a very rapid, although incomplete, inactivation (Fig. 1). At 300 μM Ca^{2+}, the time constant of the inactivating portion of current is ~0.5–1 ms at potentials positive to +40 mV. Above +50 mV, current inactivates to a steady-state level that is ~10–50% of the peak value, dependent on voltage, but largely independent of Ca^{2+}. The substantial level of steady-state sustained current indicates that both the onset and recovery of the blocking reaction are rapid. Inactivation requires the NH_2 terminus of the β3b subunit (Xia et al., 2000). Typical conductance-voltage curves measured from the peak current level, the tail current, and from the steady-state outward current are plotted in Fig. 1.

Deactivation of α + β3b Currents after Brief Activation Steps and Longer Inactivating Steps

An unusual feature of α + β3b currents is the exceedingly rapid recovery from inactivation upon repolarization (Xia et al., 2000). A repolarizing voltage step at the peak of outward current results in a tail current of amplitude essentially identical to that after a repolarization during a steady-state level of inactivation (Fig. 2). This result demands that a large number of channels that are blocked at the activation potential reopen before the peak of the tail current. In Fig. 2 A, tail currents are compared at a repolarization potential of −80 mV after either a 40-ms or a 1-ms depolarizing step to +160 mV. Peak outward current during the depolarization to +160 mV occurs somewhat before 1 ms, whereas, at 40 ms, the outward current is at the steady-state–inactivated level. Despite the differences in amount of current at +160 mV for the two traces, the current after the repolarization to −80 mV is actually somewhat greater when channels are mostly inactivated at +160 mV. When a 2-ms inactivation step is compared with the 40-ms inactivation step, qualitatively similar results are obtained (Fig. 2 B). Similar results were obtained with tail currents at −160 mV (not shown).

The fact that the tail current after the 1-ms activation step is actually smaller than that after either a 2 or 40 ms activation step presumably occurs because the peak of

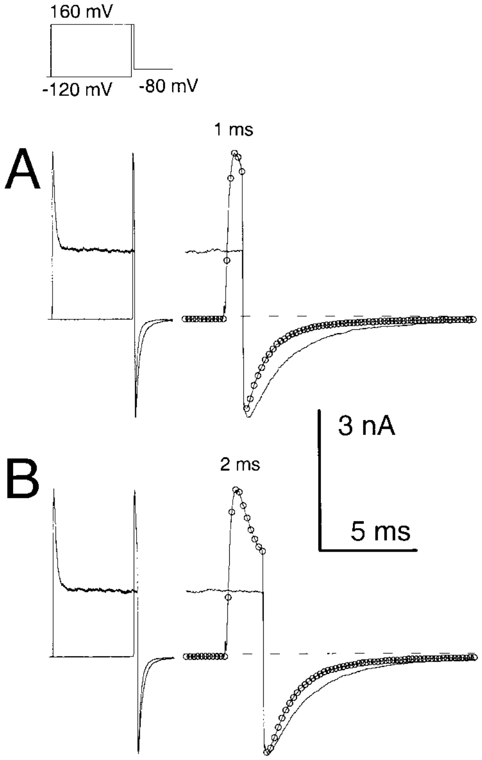

FIGURE 2. α + β3b currents rapidly recover from inactivation. Currents through α + β3b channels were activated in the presence of 10 μM Ca^{2+} by the voltage protocol shown on the top. Scale bars apply to the expanded time base traces displayed on the right. In A, traces compare tail currents after repolarization to −80 mV at the end of either a 1- or 40-ms step to +160 mV. The left traces show the complete current record, whereas the right-hand traces show the tail currents on an expanded time base. Despite the fact that outward current at the end of the 1-ms step to +160 is more than twice that at the end of the 40-ms step to +160 mV, maximal tail current amplitude after repolarization is actually larger in the latter case. Furthermore, the current decay time is markedly slower. For currents activated with the brief steps to +160 mV, symbols plot every twentieth digitized point. In B, tail currents at −80 mV are compared after either a 2-ms or a 40-ms step to +160 mV. The tail current amplitude is similar in both cases despite the fact that outward current at +160 mV differs markedly.

outward current precedes the time at which the majority of channels have entered activated states. This is a consequence of the fact that the inactivation rate exceeds the underlying rates of channel activation under some conditions (Xia et al., 2000). However, that the tail current at the time of peak outward current is less than that after the development of the steady-state blocked condition only further emphasizes the point that recovery from inactivated states to open states at potentials from −80 through −160 mV is exceedingly rapid.

Fig. 2 also shows two other notable features of these currents. First, the tail current decay appears slower following repolarization from the longer inactivating steps. Second, the tail currents following repolarization after the longer inactivating step (40 ms) can exhibit an actual initial increase in inward tail current amplitude (Fig. 2 A) or, in some cases, a shoulder that precedes the exponential decay of current in the tail. This shoulder or increase in tail current amplitude is more pronounced at more positive repolarization potentials (e.g., −80 mV).

Whatever the mechanism of the inactivation process, a large number of inactivated channels must recover very rapidly after repolarization. Yet, despite this rapid recovery, the tail currents after shorter and longer steps do not appear to decay at the same rate. As previously proposed (Xia et al., 2000), the slowing of tail current with longer inactivation steps might imply that the open channels after the longer inactivation steps are not deactivating through the same pathways as those after the shorter steps. Thus, although rapid recovery in the tail current is not necessarily unique to either Scheme 1 or Scheme 2, the fact that the tail current decay is slower with longer inactivation steps would, at first glance, suggest channels are recovering from inactivation through different open states than when they have not inactivated.

To evaluate this possibility, we now address several questions related to the tail current behavior of α + β3b. First, is the slowing of the tail current decay rate with duration of the activation step related to the inactivation process? Second, is the inward current increase during the tail current associated with the recovery from inactivation and how fast is the recovery from inactivation? Third, during repolarization to any potential, is the fast recovery from inactivation complete?

The Prolongation of Deactivation Observed for α + β3b Currents Does Not Appear To Be Related to the Inactivation Mechanism

The deactivation of currents arising from the *Slo* α subunit alone was examined at various potentials for both 10 and 300 μM for command steps ranging in duration from 0.2 to 10 ms (Fig. 3, A1 and A2 for −80 mV and 10 μM Ca^{2+}). Over this range of command steps, we observed a small, but distinct, increase in deactivation τ_d at both 10 μM Ca^{2+} and 300 μM Ca^{2+}, with some increase occurring even after the peak of outward current activation (Fig. 4). In all cases, current deactivation was reasonably described with a single exponential time course (Fig. 3 B). This prolongation was observed whether leak subtraction was used or not. With activation steps of 0.5–10 ms, the magnitude of this prolongation was on the order of 1.5–2-fold (Fig. 4, A and B).

Coexpression of α subunits with a β3 subunit lacking the inactivating NH_2 terminus (construct β3b-ΔN; Xia et al., 2000) resulted in exponentially decaying tail currents that decayed more slowly at both 10 (Fig. 3 B) and 300 μM than those arising from the α subunit

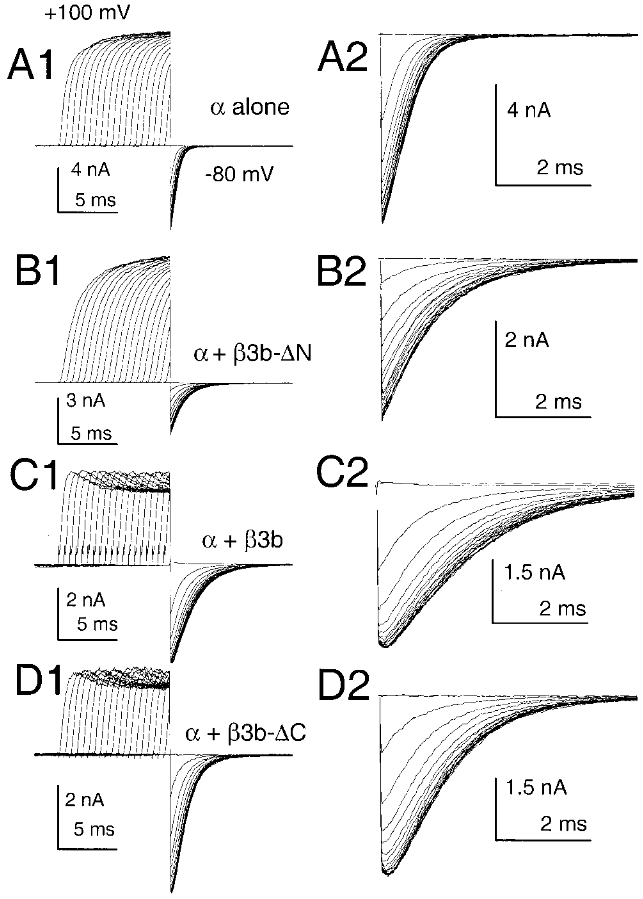

Figure 3. Slowing of deactivation as a function of activation step duration is not unique to α + β3b currents. In A1–D1, outward current was activated with 10 μM Ca^{2+} by a step to +100 mV from a holding potential of −120 mV. For each sweep, the step to +100 mV was varied from 0 to 9.5 ms in 0.5-ms increments, before a repolarizing step to −80 mV. Currents resulted from the following constructs: (A) α alone; (B) α + β3b-ΔN; (C) α + β3b; and (D) α + β3b-ΔC. For these constructs, a direct step to −80 mV from −120 mV results in minimal inward current activation. A2–D2 show the tail currents on an expanded time base. For α alone (A2) and for α + β3-ΔN (B2), tail currents become slower with command step duration, but the decay qualitatively appears to begin a single exponential time course immediately after the repolarizing step. For α + β3b (C) and α + β3b-ΔC (D), tail current decay also appears to slow with command step duration. However, in contrast to the noninactivating currents, as the command step is increased in duration there is an increase in a shoulder of tail current that precedes the onset of an exponentially decaying current. For all panels, a P/N leak subtraction procedure was used (see materials and methods).

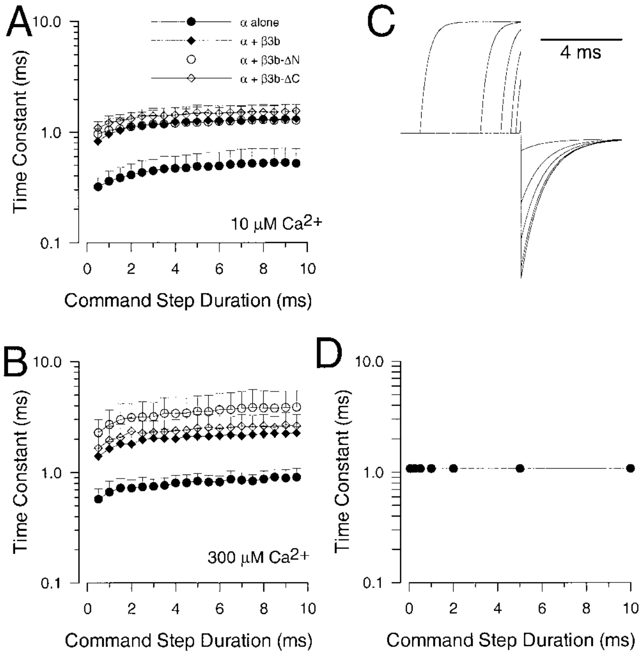

Figure 4. The dependence of tail current deactivation time constant on command step duration. The protocol shown in Fig. 3 was used to activate tail currents at different times after a step to +100 mV. In all cases, single exponential functions were fit to the decaying phase of the tail currents. In A, means and standard deviations of deactivation time constants measured with 10 μM Ca^{2+} are plotted as a function of activation step duration. Each construct exhibits a similar factional change in decay time as the command step is increased from 0.5 to 9.5 ms. In B, time constants and standard deviations were determined in 300 μM Ca^{2+}. Prolongations are similar for each of the constructs. In both A and B, each point corresponds to a minimum of five patches. In C, a protocol similar to that used in Fig. 3 was simulated for a MWC 10-state activation model using rates similar to those given in Table I derived from of Cox et al. (1997). In D, tail current time constants measured from C are plotted as a function of command step duration.

alone. Like the α subunit alone, α + β3b-ΔN currents exhibited a slight slowing in τ_d as a function of activation step duration (Fig. 4). When deactivation was examined for either wild-type α + β3b currents (Fig. 3 C) or for α + β3b-ΔC (Fig. 3 D; a construct lacking the β3b-ΔC), there was also a 1.5–2-fold slowing of τ_d as command step duration was increased. However, in contrast to the noninactivating currents resulting from α alone or α + β3b-ΔN, both α + β3b and α + β3b-ΔC currents exhibited an unblocking component in their tail currents (Fig. 3, C and D). The magnitude of this unblocking component increased as the duration of the activation step was increased.

These results indicate that a 1.5–2.0-fold slowing of τ_d occurs with increases in activation step duration for all four types of currents. Thus, the slowing of deactivation is unrelated to the inactivation mechanism itself. Here, we make no attempt to provide an explanation for this slowing, but note that a simple voltage-dependent MWC model (Cox et al., 1997) does not predict an activation-dependent slowing of deactivation (Fig. 4, C and D). In our experiments, the occurrence of activation-dependent slowing of deactivation was not dependent on current amplitude among different patches, and also occurred with 300 μM Ca^{2+} in which 50 μM of the crown ether Ba^{2+} chelator, 18C6TA, was included (not shown).

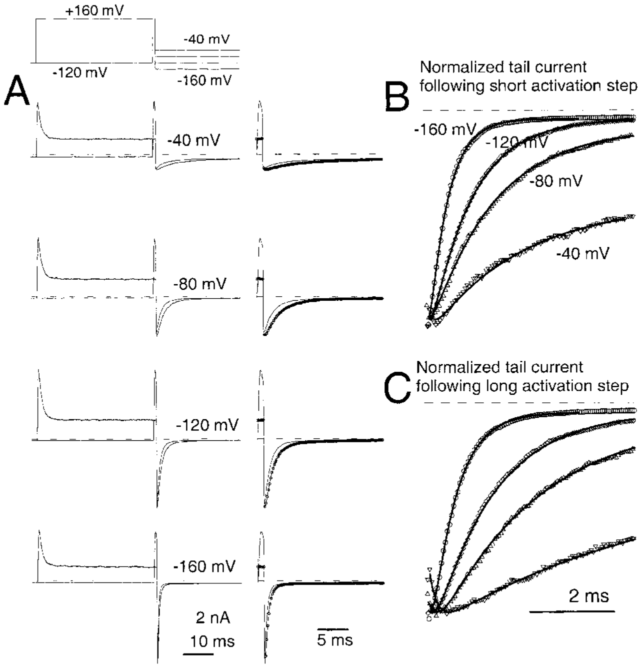

FIGURE 5. Inactivation is associated with the appearance of a rapid unblocking component in the tail current. In A, a protocol similar to that used in Fig. 2 was used to examine tail currents at repolarization potentials of −40, −80, −120, and −160 mV with 10 μM Ca^{2+}. In the right-hand traces of A, points show every twentieth digitized value for currents resulting from a 40-ms activation step. In B, normalized tail currents after the 2-ms activation step (from A) are shown for the indicated repolarization potentials. Only every fifth digitized value (50 μs) is displayed. At the most positive repolarization potential (−40 mV), there is a pronounced lag before the tail current begins to decay in an exponential fashion. At more negative potentials, after a brief capacitative current, the current begins an exponential decay fairly rapidly. Lines correspond to a fitted two exponential function, $A1 \cdot \exp(-t/\tau_u) + A2 \cdot \exp(-t/\tau_d)$ + offset, where τ_u corresponds to an unblocking relaxation, and τ_d corresponds to the deactivation time course. At −160 mV, $\tau_u = 0.087$ ms and $\tau_d = 0.44$ ms; at −120 mV, $\tau_u = 0.113$ ms and $\tau_d = 0.98$ ms; at −80 mV, $\tau_u = 0.172$ and $\tau_d = 1.50$ ms; and at −40 mV, $\tau_u = 0.134$ and $\tau_d = 2.16$ ms. In C, normalized tail currents activated after a 40-ms activation step are shown over the same range of repolarization potentials. At both −40 and −80 mV, there is a distinct increase in tail current after the capacitative transient. At both −120 and −160 mV, the shoulder of current before the onset of exponential decay is more pronounced than in B. Open symbols again show every fifth digitized data value, whereas solid lines correspond to a two exponential fit to the decay time course. Fitted values were as follows: at −160 mV, $\tau_u = 0.128$ ms and $\tau_d = 0.57$ ms; at −120 mV, $\tau_u = 0.173$ ms and $\tau_d = 1.42$ ms; at −80 mV, $\tau_u = 0.232$ ms and $\tau_d = 2.415$ ms; and at −80 mV, $\tau_u = 0.183$ and $\tau_d = 5.64$ ms.

Fig. 4 shows that τ_d is similar for both α + β3b and α + β3b-ΔN currents. This indicates that the time course of current deactivation is not markedly influenced by any molecular transitions requiring the NH_2-terminal inactivation domain. This result indicates that the rate limiting steps in current deactivation are not coupled to transitions involved in recovery from inactivation. This assertion is also supported by experiments below in which the NH_2 terminus is enzymatically removed with trypsin.

With an Intact Inactivation Domain, Tail Currents Exhibit a Fast Unblocking Process

The results in Fig. 2 show that recovery from inactivation for α + β3b currents must occur very rapidly, since the tail current conductance at the earliest discernible times greatly exceeds the steady-state conductance at positive potentials. However, as noted above, for both α + β3b and α + β3b-ΔC currents, at more positive deactivation potentials following the initial essentially instantaneous recovery in current amplitude, there is a secondary shoulder or slight increase in inward tail current (Figs. 2 and 3). This is evaluated more explicitly in Fig. 5. After repolarization to either −40 or −80 mV, there is a nonohmic step to an initial tail current amplitude that shows a secondary increase reaching a peak in <1 ms. At more negative potentials (−120 and −160 mV), after the initial decay of uncompensated patch capacitance, there is only a shoulder that precedes the onset of deactivation. Tail currents recorded after brief activation steps (Fig. 5, A and B) show a brief voltage-dependent shoulder before the onset of deactivation, although only at −40 mV is there any indication of an actual unblocking process before the peak tail current. Comparison of tail currents resulting from constructs containing the β3b inactivation domain (α + β3b and α + β3b-ΔC) to those lacking the inactivation domain (α alone and α + β3b-ΔN) indicate that this unblocking process is unique to channels exhibiting inactivation (Fig. 3).

For better comparison, tail currents were normalized to their peak amplitudes for either the shorter activation steps (Fig. 5 B) or longer activation steps (Fig. 5 C). With 10-μs sampling and 10 kHz filtering, the solid lines (Fig. 5, B and C) show the best fit of a two exponential function to each of the tail currents. Over the range of −40 mV to −160 mV, for the examples shown, the fitted values for the initial, rapid unblocking time constant (τ_u) ranged from ∼250 μs at −40 mV to ∼120 μs at −160 mV. This 100–250-μs unblocking relaxation is too slow to account for the "instantaneous" unblocking of current that produces the nonohmic discrepancy between the steady-state conductance and the initial conductance of the tail currents.

These results indicate that, although the slowing of τ_d with command step duration appears unrelated to the inactivation process, there are two components of the inactivation process that are discernible in the tail currents: a nonohmic, almost instantaneous unblocking of channels, followed by a rapid unblocking relaxation (τ_u) or shoulder in the tail current. The shoulder in the tail currents is not observed in the absence of the NH_2-terminal inactivation domain.

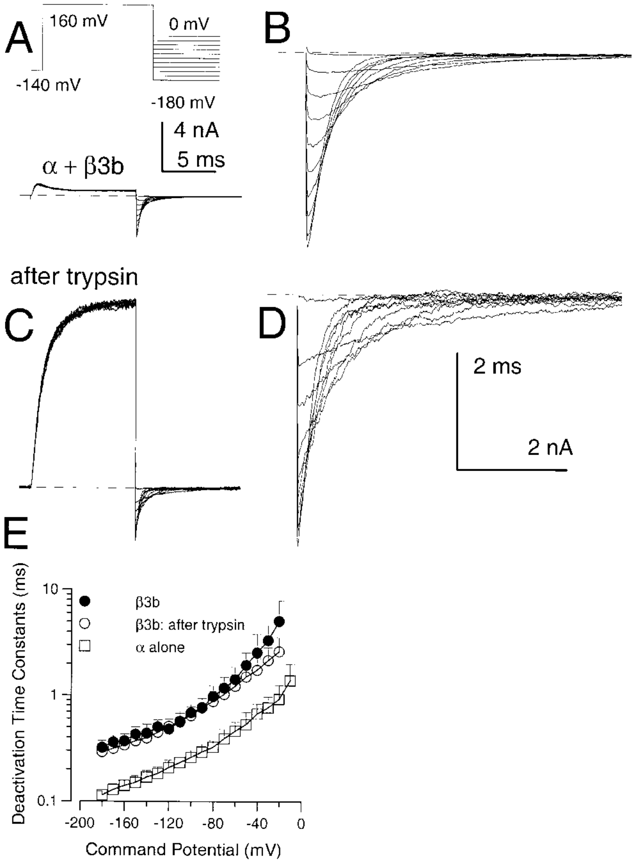

Figure 6. Effects of trypsin on α + β3b currents. In A, currents in an inside-out patch expressing α + β3b channels were activated by the indicated voltage protocol with 10 μM Ca^{2+}. In B, the tail currents at potentials from 0 mV to −180 mV are displayed at higher magnification. In C, trypsin was briefly applied to the same patch shown in A resulting in removal of inactivation, whereas D shows the tail currents after trypsin at higher magnification. After trypsin, peak outward current at +160 mV appears to activate more slowly and is markedly larger. In contrast, tail current amplitudes exhibit a more modest increase after trypsin. The calibration bar in A also applies to C, while B and D share a calibration bar. Tail current amplitude at more positive repolarization potentials exhibits a larger increase following trypsin than those at more negative potentials. After trypsin application, the tail current decay follows a relatively simple exponential time course, whereas, before trypsin, there is a brief rising phase. In E, time constants of deactivation (τ_d) are plotted for α + β3b currents before (●) and after (○) trypsin and compared with τ_d for currents arising from α alone (□). Tail currents for intact α + β3b were fit with a two exponential function to approximate the fast unblocking shoulder of current and then the deactivation of current. Points show means and standard deviations for at least four patches.

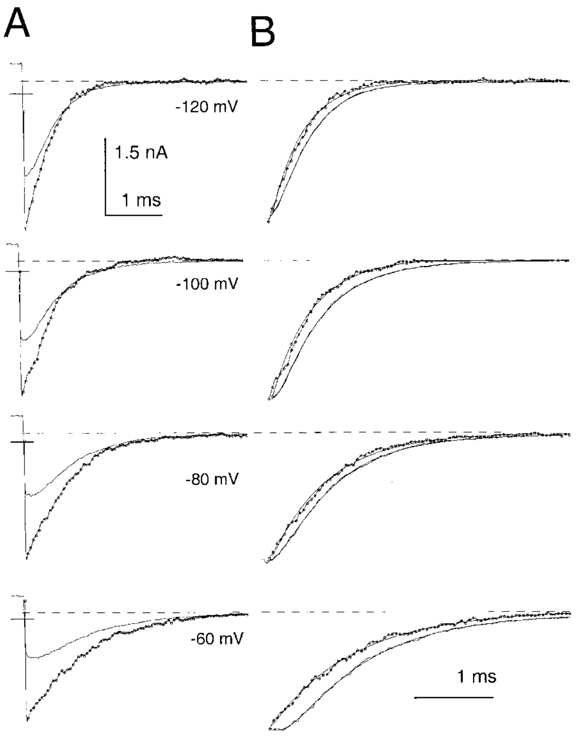

Figure 7. Trypsin removes the unblocking relaxation observed in α + β3b tail currents. In A, panels from top to bottom compare tail currents at the four indicated repolarization potentials, before and after (line with points) trypsin application. Despite the extensive unblocking that occurs during repolarization, the ability of trypsin to increase the tail current amplitude suggests that even at negative potentials some voltage-dependent block of channels persists. At −120 mV, tail current amplitudes before trypsin are ~70% of those after trypsin application. For the traces after trypsin application, the points correspond to every fifth digitized value. The horizontal bars overlaid on the rising phase of the tail currents indicate the calculated level of tail current expected at the repolarization potential assuming an instantaneous ohmic step from the residual level of current at +160 mV. A small segment of the steady-state–inactivated current at +160 mV is shown for the traces before trypsin application. Filter, 10-kHz bandwidth; sampling period, 10 μs. In B, each pair of traces was normalized to the same peak amplitude. For the trace obtained before trypsin application, the deactivation time course was fit with the following two exponential function: $A1 \cdot \exp(-t/\tau_u) + A2 \cdot \exp(-t/\tau_d) + \text{offset}$. At −120, −100, −80, and −60 mV, the unblocking relaxations were 0.18, 0.13, 0.20, and 0.24 ms, respectively, whereas the subsequent deactivation time constants were 0.40, 0.57, 0.71, and 0.98 ms, respectively. After trypsin, a fit of $A1 \cdot \exp(-t/\tau_d) + C$ yielded time constants of 0.42, 0.52, 0.74, and 1.06 ms.

Trypsin-mediated Removal of Inactivation Removes the Unblocking Relaxation in the Tail Current, but Does Not Alter the Tail Current Decay Rate

The similarity in τ_d (once the unblocking relaxation is complete) for α + β3b, α + β3b-ΔC, and α + β3b-ΔN currents suggests that similar molecular transitions govern the deactivation time course in all cases. This requires either that transitions into and out of blocked states do not occur during the decay phase of the tail currents or that such transitions do not impede channel closure. We next compared tail currents resulting from activation of α + β3b channels with 10 μM Ca^{2+} before (Fig. 6, A and B) and after removal of inactivation by trypsin (Fig. 6, C and D). After trypsin, outward current at +160 mV exhibits a slower apparent activation time course and peak outward current is increased over 10-fold. Tail currents after trypsin exhibit a much smaller increase in amplitude, and no longer show the unblocking relaxation characteristic of the intact α + β3b currents. This indicates that the unblocking relaxation in the tail currents requires an intact inactivation mechanism. However, the trypsin-induced increase in tail current amplitude suggests that, even though unblock after repolarization is rapid, it is not complete, even at the most negative repolarization potentials.

The effects of trypsin on tail currents are shown in more detail in Fig. 7. Comparison of the peak tail current amplitudes before and after trypsin (Fig. 7 A) shows that, when inactivation is intact, although repolarization produces an extremely rapid unblocking of current, the peak tail current amplitude is still reduced in a voltage-dependent fashion. At −60 mV, trypsin results in an over twofold increase in the peak tail current amplitude, whereas at −120 mV, trypsin results in an ~1.5-fold increase. This contrasts to the almost 10-fold increase in current seen at +160 mV. The tail current traces were normalized and plotted along with single (after trypsin) or two (before trypsin) exponential fits to the decay time course (Fig. 7 B) to emphasize that before trypsin, there is an initial unblocking component in the tail current, which is removed by trypsin. A comparison of τ_d before and after trypsin shows that removal of inactivation does not alter the deactivation rate (Fig. 6 E). To emphasize that the 100–250-μs unblocking relaxation does not account for the nonohmic instantaneous unblocking, the ohmic level of current expected at any deactivation potential is indicated in Fig. 7 A for α + β3b currents. Based on the discrepancy between the current amplitude at the earliest times of the tail current and an assumed ohmic instantaneous current level, a large percentage of blocked channels have already unblocked during the repolarizing step before the onset of the 100–250-μs unblocking relaxation.

One cautionary comment is that there are unusual nonohmic aspects of instantaneous currents arising from the α + β3b subunits that are observed after removal of the NH_2 terminus. As will be seen below, the underlying intrinsic instantaneous current-voltage (I-V) properties conferred by the β3b subunit exhibit marked outward rectification, in marked distinction to the inward rectification produced by rapid block by the NH_2 terminus. Thus, if we assume that channels with the intact NH_2 terminus behave similarly, the discrepancy between the predicted level of current after the repolarizing voltage step and the observed instantaneous current after unblocking would be even greater. Irrespective of the impact of the outward rectification, it is clear that the tail currents upon repolarization during steady-state inactivation exhibit both an instantaneous component of unblocking, and then a slower time-dependent unblocking.

Do any observations presented to this point place any constraints on the type of model that might account for the results? The existence of two distinct unblocking components in the tail currents argues that at least two steps are involved in the inactivation process, which is consistent with Scheme 2, but not Scheme 1. On the other hand, the absence of any marked effect of the NH_2-terminal–mediated blocking mechanism on τ_d is at variance with both linear blocking schemes.

Properties of Instantaneous Current-Voltage (I-V) Curves after Recovery from Steady-state Inactivation

As another approach to evaluation of the rapid recovery process, we examined the amplitude of tail currents over potentials from −180 mV through +180 mV after

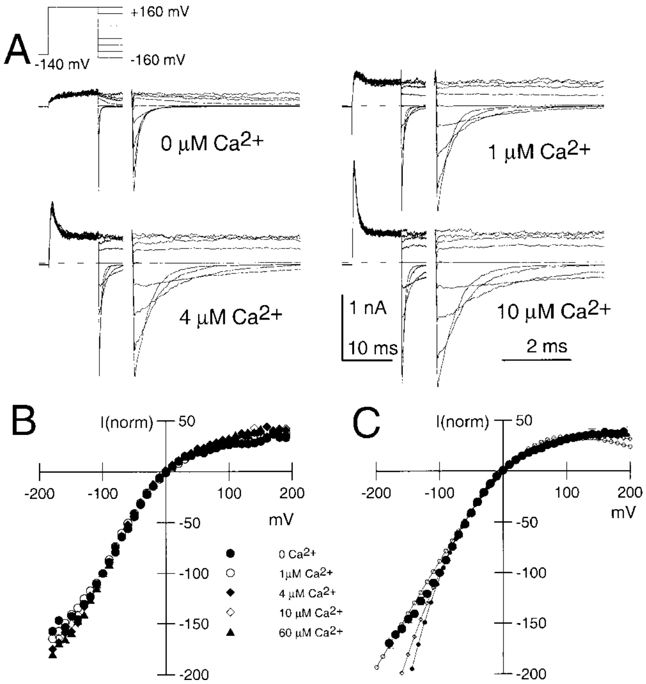

FIGURE 8. Properties of instantaneous current-voltage (I-V) curves following repolarization from a steady-state–inactivated condition. In A, currents were activated by the indicated voltage protocol at various Ca^{2+} (0, 1, 4, and 10 μM Ca^{2+}). For all Ca^{2+}, there is a large, immediate nonohmic increase in tail current indicative of rapid unblocking from inactivation. In B, the current was measured 100 μs after the nominal time of the repolarizing voltage step and normalized to the current measured with the step to −100 mV. The shape of the I-V curve is identical for all Ca^{2+}. In C, the mean and standard deviation for the instantaneous I-V curve from five patches at 10 μM Ca^{2+} are plotted, along with the best fit of Eq. 5. For the fit with solid circles all values were unconstrained yielding G_{max} = 30.5 ± 24.0; $K_2(0)$ = 51.7 ± 49.44 and Q_2 = 0.154e ± 0.020e. For the fit with diamonds, G_{max} was constrained to 2.0 with $K_2(0)$ = 2.27 ± 0.045 and Q_2 = 0.209e ± 0.005e. For the open circles, G_{max} was constrained to 1.0 with $K_2(0)$ = 0.504 ± 0.07 and Q_2 = 0.341e ± 0.03e.

inactivation at +160 mV (Fig. 8 A). To avoid assumptions about the time course of the decay process, the current amplitude at a time point 100 μs after the nominal time of the repolarizing voltage-step was measured. Current amplitudes were normalized to the current measured at −100 mV. These instantaneous I-V curves were essentially identical at all Ca^{2+} concentrations (Fig. 8 B), and exhibited strong inward rectification.

Results so far suggest that the initial tail current amplitude reflects something about the fractional recovery from inactivation. The fact that trypsin results in an increase in tail current amplitude shows that the unblocking process is not complete. Thus, the instantaneous recovery to a new partially blocked level would imply that the initial tail current amplitude reflects a new voltage-dependent equilibrium between open and inactivated states. Following this idea, here we analyze the properties of the instantaneous I-V curve in terms of Scheme 2, in which we propose that the instantaneous unblock reflects the rapid equilibration of channels between states O^*_n and I_n. By assuming for the moment that any curvature in the instantaneous I-V arises from rapid development of a new voltage-dependent equilibrium between O^*_n and I_n, we can extract some estimates of the properties of that proposed equilibrium and ask whether the shape of the I-V curve is consistent with other aspects of our results.

As a first approximation, we assume that, at +160 mV, channels are in a rapid equilibrium between states O^*_n and I_n with occupancy of states (O_n) assumed to be negligible. After repolarization, the new conductance at any potential would be given solely by the new equilibrium between O^*_n and I_n. Therefore, an estimate of the relative current (I) at any potential (V) is given by:

$$I(V) = V \cdot G_{max} \cdot k_u(V)/k_u(V) + k_b(V).$$

Since the ratio I/O* is given by $K_2(V) = k_b(V)/k_u(V)$,

$$I(V) = V \cdot G_{max}/(1 + K_2(V)).$$

With $K_2(V) = K_2(0) \cdot \exp(Q_2FV/RT)$,

$$I(V) = V \cdot G_{max}/1 + K_2(0) \cdot \exp((Q_2FV)/RT). \quad (3)$$

Although the three parameters provided by Eq. 3 (G_{max}, $K_2(0)$, and Q_2) are not well constrained by the shape of the curve in Fig. 8 C, evaluation of the data in terms of Eq. 3 can place some limits on this postulated equilibrium. Points were fit over the range of −90 mV through +160 mV. Values at more negative potentials are likely to be underestimated because of more rapid deactivation at those potentials. Fig. 8 C shows the result of three cases: (1) fitting with all parameters unconstrained; (2) fitting with G_{max} constrained to be maximal at −100 mV; and (3) fitting with G_{max} constrained to twice the value observed at −100 mV. Case 2 corresponds to the assumption that all channels return to open states at −100 mV. Case 3 is in accordance with the observation that the tail current amplitude approximately doubles at −100 mV after trypsin application. In this case, $K_2(0) = 2.27 \pm 0.045$ and $Q_2 = 0.21 \pm 0.005$ (Fig. 9 A).

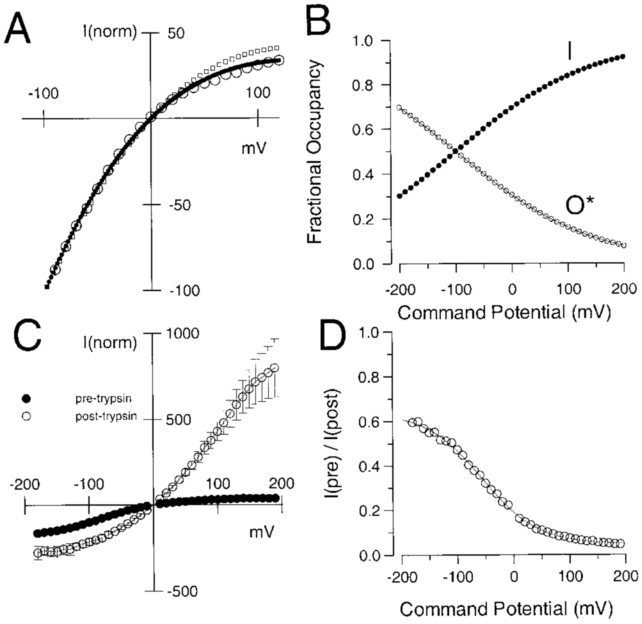

FIGURE 9. Despite fast unblocking, α + β3b tail currents exhibit a residual voltage-dependent blockade at negative potentials. In A, the instantaneous I-V curve obtained with 10 μM Ca^{2+} (○) is replotted (from Fig. 8 C) along with the fit for the case where G_{max} was constrained to 2.0 (●). Predictions based on the values given in Table I and used for the simulations in Fig. 15 are also shown (□; also see *Online Supplemental Materials* available at http://www.jgp.org/cgi/content/full/117/6/583/DC1). In B, based on the values for $K_2(V)$ obtained from the fit shown in A, fractional occupancy in O^*_n (○) and I_n (●) was calculated and plotted as a function of the potential at which the tail current was measured. In C, tail current amplitudes (normalized to −100 mV) were measured for three patches before (●) and after (○) removal of inactivation with trypsin. In D, the ratio (○) of tail current amplitude at 100 μs before trypsin application to that after removal of inactivation is plotted as a function of repolarization potential. Note the correspondence of these values to those for O^*_n in panel B. The solid line is a fit of the following equation:

$$f(V) = \frac{f_{max}}{1 + K(0)\exp^{\frac{-zFV}{RT}}},$$

where $f_{max} = 0.613$, $K(0) = 3.32$ and $z = -0.503$.

Since the ratio of I/O* at a given potential is given by $k_b(V)/k_u(V)$ or $K_2(V)$, the relative occupancy of O* and I at different voltages can be calculated (Fig. 9 B). This analysis suggests that occupancy of blocked states is still appreciable at potentials negative to 0 mV, consistent with the effects of trypsin on the tail current amplitude at negative potentials (Fig. 6 C). At each voltage, the amplitude of the tail current before and after trypsin application, therefore, was determined (Fig. 9 C) along

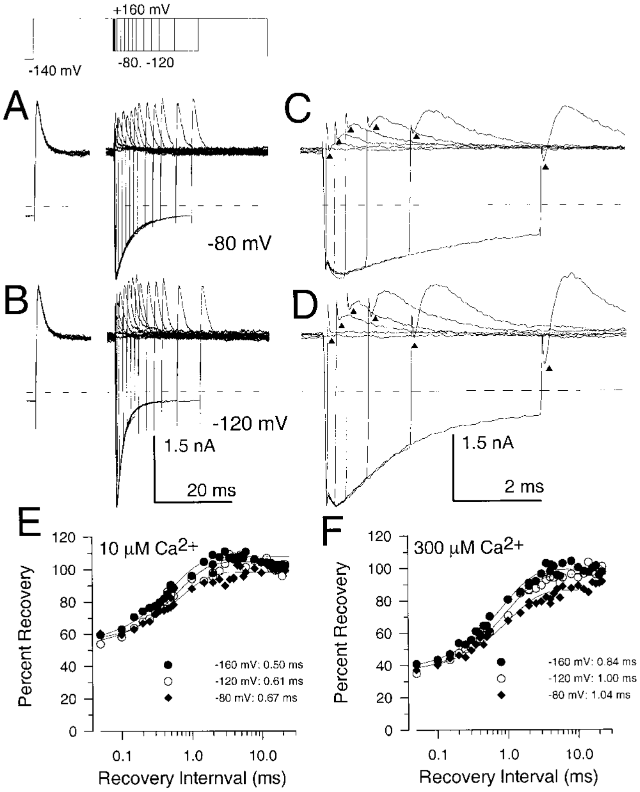

FIGURE 10. Paired pulse recovery protocols reveal a slow recovery from inactivation despite nearly complete recovery from block in the peak tail current. Recovery from inactivation was assessed using the indicated voltage-protocol. The duration of the initial inactivating step to +160 mV was 40 ms. Recovery steps were varied from 50 μs to 40 ms, although not all are displayed. In A and B, currents were activated with 10 μM Ca^{2+}, and the recovery potential was either −80 mV (A) or −120 mV (B). In C and D, selected traces from A and B are shown on a faster time base. For faster time records, traces correspond to recovery intervals of 0, 0.05, 0.25, 0.5, 1.0, 2.0, and 5.0 ms. Triangles draw attention to the amount of outward current present immediately after completion of the capacitative transient associated with the second test step to +160 mV. For brief recovery intervals, this instantaneous level of current is identical to the steady-state level of current at +160 mV. With longer recovery intervals, the amplitude of the instantaneous current indicated by the triangles increases even as the tail current at −80 or −120 mV is beginning to decrease. The dotted line indicates the zero current level. In C, the percent recovery measured from the paired pulse protocol is plotted as a function of the recovery duration at each of three recovery potentials with 10 μM Ca^{2+}. The solid lines represent single exponential fits to the recovery time course. At −80 mV, a two exponential fit gave a somewhat better description of the recovery time course, but, at more negative potentials, a two exponential time course did not substantially improve the quality of the fit. At −160 mV, τ_r = 0.5 ms; at −120 mV, τ_r = 0.61 ms; and at −80 mV, τ_r = 0.67 ms. In D, the time course of recovery in the paired pulse protocol is shown for 300 μM from the traces in Fig. 11 B. At −160 mV, τ_r = 0.84 ms; at −120 mV, τ_r = 1.00 ms; and at −80 mV, τ_r = 1.04 ms.

with the ratio of tail current before and after trypsin (Fig. 9 D). This fractional unblock revealed by trypsin (Fig. 9 D) correlates well with the proposed fractional occupancy of states (O^*_n) plotted in Fig. 9 B, which was calculated from the curvature of the instantaneous I-V curve. It should also be noted that, after trypsin, the instantaneous I-V curve exhibits an unusual outward curvature. This is an intrinsic property of channels arising from α + β3b coexpression and is unrelated to any secondary effect of trypsin (Zeng et al., 2001).

To this point, the results and analysis indicate the following. First, when channels are in a steady-state–inactivated condition, repolarization results in an exceedingly rapid unblocking process, exhibiting two distinct components. Unblock is seen both as a nonohmic increase in conductance upon repolarization, and followed at some potentials by an unblocking relaxation of 100–250 μs. The presence of these two components are generally consistent with Scheme 2, but inconsistent with Scheme 1. Second, τ_d is not influenced by blocking transitions. Third, both the curvature in the instantaneous I-V curve and the effects of trypsin on tail current amplitude indicate that, despite the rapidity of unblocking, even at negative potentials a new steady-state, voltage-dependent level of block is rapidly achieved. Our analysis of the inward rectification of the instantaneous I-V curves in terms of Scheme 2 will require additional validation, as presented below. In fact, some aspects of this analysis would apply to any model, including Scheme 1, in which rectification results from a very rapid voltage-dependent equilibrium between open and closed states. However, the presence of two unblocking components in the tail currents suggests that Scheme 1 is not suitable in the present case.

Paired Pulse Recovery Protocols Also Reveal Multiple Components of Recovery from Inactivation

A standard approach to defining kinetic properties of an inactivation process is to examine recovery from inactivation using a paired pulse protocol. This sort of protocol uses a variable recovery interval at a repolarizing potential to define the fractional recovery from inactivation. For Scheme 1, if upon repolarization most channels rapidly return to states O_n, a subsequent depolarizing voltage-step at the peak of the tail current would be expected to result solely in an ohmic step of current corresponding to the number of channels still open during the tail current. The ohmic step would then be followed by a subsequent time-dependent inactivation of open channels governed by the O_n to I_n transitions. With longer recovery intervals, the ohmic current would be expected to decrease, as more channels have returned to closed states (C_n). In contrast, the predictions from Scheme 2 are more complex.

Such an experiment is shown in Fig. 10. After development of steady-state inactivation at +160 mV, the effect of recovery steps of different duration on current activation during a subsequent step to +160 mV was examined. Recovery was examined with 10 μM Ca^{2+} at either −80 mV (Fig. 10 A) or −120 mV (Fig. 10 B). Quite remarkably, with short recovery intervals (e.g., 50–250 μs), the subsequent depolarization to +160 mV results in currents that show only small recovery above the previous steady-state–inactivated level at +160 mV. Thus, despite the fact that a large number of channels recover almost instantaneously to open states during the repolarization, these channels become almost immediately blocked upon depolarization after short duration recovery steps. With longer recovery intervals, peak current activated during the second test step gradually recovers to the amplitude of the first test step with a time constant on the order of 0.5–1.5 ms depending on voltage and Ca^{2+} (Fig. 10, C and D).

The recovery process is seen more clearly with the faster time base traces in Fig. 10, A and B. For the shortest recovery interval (50 μs), a subsequent depolarization to +160 mV results in a return to almost the same steady-state–blocked level of current (indicated by a triangle) once the brief capacitative transient is complete. With longer recovery periods, the level of current after completion of the capacitative transient slowly increases with increases in repolarization duration. In addition, there begins to be a time-dependent activation of outward current, and then the slower inactivation of current. With even longer recovery periods, the step change in current diminishes as the amount of current that exhibits time-dependent activation and inactivation increases. Two aspects of the current levels marked by the triangles should be noted. First, given the amount of current present in the tail currents at either −80 or −120 mV, the level of current during the subsequent step to +160 mV is markedly nonohmic, indicating that channels that are open during the tail current have reblocked instantaneously during the depolarization. Second, although there is some correspondence between the unblocking observed in the tail current and the slow increase in the instantaneous current level (triangles) after the depolarization, the instantaneous currents actually reach a peak value that lags the peak of the tail current. Thus, the instantaneous current seen at +160 mV does not simply reflect the total number of channels open during the tail current, but must reflect something about the particular open states occupied at different times during the tail current.

These observations can be explained in terms of Scheme 2 as follows. During the depolarizing step, channels are in rapid equilibrium between the conducting, preinactivated states (O^*_n), and the nonconducting, inactivated states (I_n). Upon repolarization, channels rapidly reach a new equilibrium between O^*_n and I_n, with greater occupancy of O^*_n. However, when channels are in O^*_n, a subsequent depolarization causes an almost instantaneous return to the original voltage-dependent equilibrium between O^*_n and I_n, because of the rapid rates of the transitions between O^*_n and I_n. Thus, the original steady-state current level at +160 mV is reached immediately. With longer recovery times, channels from O^*_n will return to normal open states, O_n. This will result in a small, time-dependent increase in the total number of channels in open states, resulting in the unblocking and shoulder in the tail

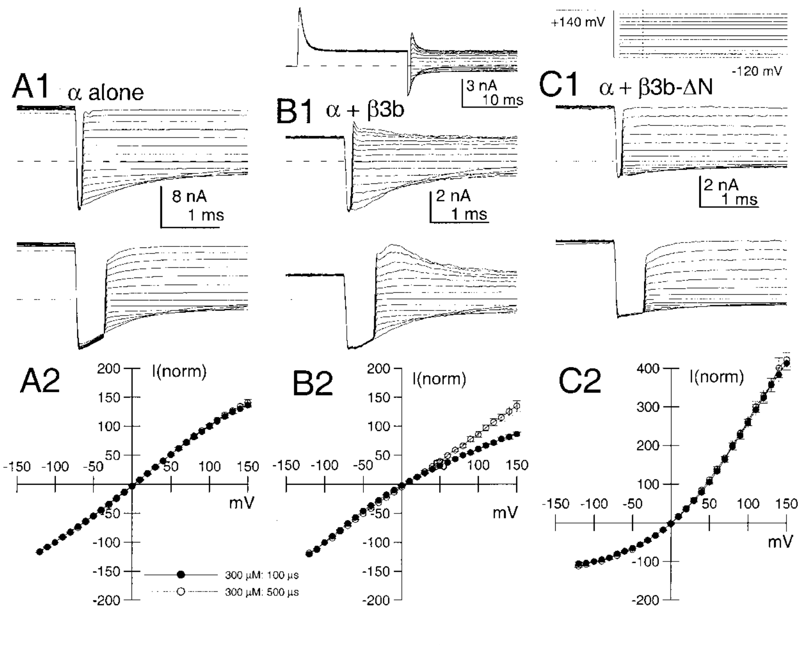

FIGURE 11. α + β3b channels pass through different open states during recovery from inactivation. Currents displayed in A–C were evoked with the portion of the voltage protocol shown above C. An example of the full current waveform (for α + β3b) is shown above B1. Steady-state current activation was achieved at +140 mV, and the patch was stepped to −120 mV for either 100 μs (top traces) or 500 μs (bottom traces) before a subsequent depolarization to potentials between −120 and +140 mV. In A1, traces show currents resulting from only α subunits activated with 300 μM Ca^{2+}. The current amplitude was measured at a time point 80 μs after the nominal time of the final voltage step. In A2, instantaneous current amplitudes were normalized for five patches to current amplitudes elicited at +100 mV with 300 μM. At 300 μM Ca^{2+}, current has decayed ~25% more at 500 μs than at 100 μs. Similar normalized I-V curves were obtained with 10 μM Ca^{2+}. In all cases, the instantaneous I-V curve is essentially linear from −100 through +100 mV. In B1, similar tests were performed on α + β3b currents with 300 μM Ca^{2+}. Note the larger amplitude of instantaneous current at positive voltages after 500 μs at −120 mV. In B2, instantaneous current amplitudes were normalized as in A2 for five patches with 300 μM Ca^{2+}. Instantaneous currents activated at 100 μs are inwardly rectifying, whereas those activated at 500 μs approach linearity. In C1, a similar experiment was done on patches expressing α + β3b-ΔN. In C2, the instantaneous I-V curves obtained with 300 μM are similar for both 100- and 500-μs recovery steps.

currents. For those channels in O_n, a subsequent depolarization would be expected to result in an ohmic step of current, before those channels subsequently enter O^*_n, and then inactivate. Only as the fraction of channels reentering C_n increases will the slower time-dependent activation and inactivation become more pronounced. In contrast, Scheme 1 predicts that, after unblocking associated with even the shortest repolarizations, the subsequent depolarization should result in an ohmic step in outward current, followed by a 1-ms blocking relaxation. This is clearly not observed.

Kinetically, the number of blocking and unblocking components observed in our data requires a minimum of four distinct sets of states. Is it possible that a model containing two nonconducting inactivated states $(C \rightleftharpoons O \rightleftharpoons I_1 \rightleftharpoons I_2)$ would account equally well for the results? The simple answer is no. The characteristics of the unblocking process require that the blocking scheme contain at least two distinct types of open states. One type of open state is indicated by a component of current that undergoes an ~1-ms relaxation to the inactivated condition. A second type of open state is indicated by the fact that there exists a component of current that exhibits an essentially instantaneous block and unblock. This is shown explicitly in the next section.

Instantaneous Macroscopic I-V Curves at Different Times during the Tail Currents Also Indicate that α + β3b Channels Occupy Unique Open States

We have just proposed that, at different times in the tail current, the relative occupancy of states O_n and O^*_n varies. Because of the rapid block of channels in states O^*_n, instantaneous I-V curves arising from channels in O^*_n would be expected to differ from instantaneous I-V curves arising from channels in state O_n. The relative curvature of the instantaneous I-V curve, therefore, should differ at early and later times in the tail current, depending on the relative occupancy of each proposed open state. If a conventional type of blocking model involving a single open state were correct, the shape of the instantaneous I-V should be unchanged.

To test this idea, depolarizations to potentials between −120 and +160 mV with 300 μM Ca^{2+} were applied at either 100 or 500 μs after a repolarization to −160 mV (Fig. 11). Current levels at 100 μs after the nominal application of the depolarizing voltage-step were measured and plotted for α alone and α + β3b. Currents from the α subunit alone exhibited a largely linear instantaneous I-V after either 100- or 500-μs repolarizing steps (Fig. 11 A). In contrast, α + β3b currents exhibited the expected inward rectification, but the rectification was less pronounced after the 500-μs step to −160 mV (Fig. 11 B). This supports the idea that the relative occupancy of channels in different open states has changed during the tail current. Specifically, the fraction of channels in states O_n has increased relative to the fraction in states O^*_n. A similar experiment was done for currents arising from α + β3b-ΔN (Fig. 11 C). The instantaneous I-V curve exhibited a nonlinear outwardly rectifying behavior (Zeng et al., 2001), but the shape of the I-V curve was identical after either 100- or 500-μs repolarizing steps. Similar outward rectification in the instantaneous I-V was also observed after trypsin-mediated removal of inactivation of α + β3b channels (Fig. 9 C).

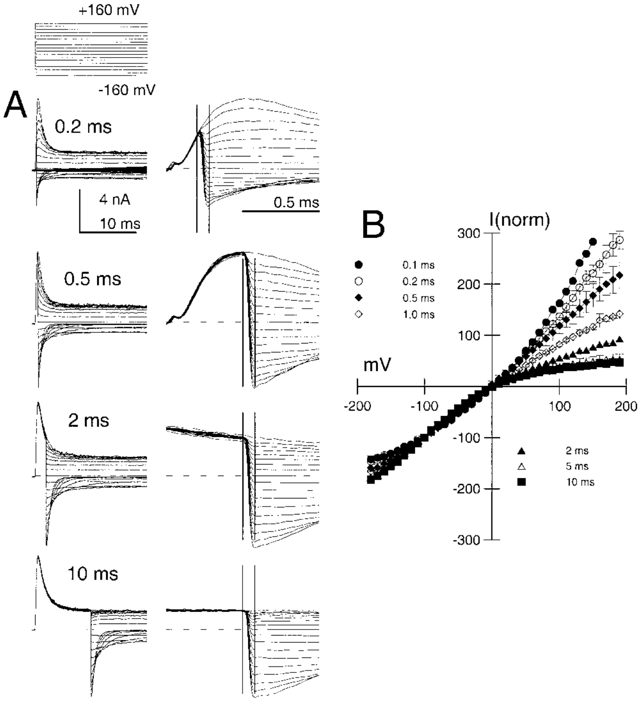

FIGURE 12. Instantaneous I-V curves for α + β3b currents change as a function of duration of the activation step. In A, α + β3b currents were activated with 10 μM Ca^{2+} with the voltage protocol shown on the top, except the command step duration was varied as indicated on the figure. Traces on the right are faster time base records of the traces on the left focusing on the properties of currents after repolarization. The vertical bars show the time points at 0 and 80 μs relative to the nominal time of the voltage-step. For the 200-μs activation step, note that currents after repolarization to voltages negative to zero are more closely spaced than those positive to zero, indicative of the intrinsic outward rectification. Sampling period, 10 μs; filter, 10 kHz. In B, current amplitudes were measured at the 80-μs time point after repolarization for each voltage, normalized to the trace at −100 mV, and plotted as a function of repolarization potential.

The novel change in instantaneous I-V curves as a function of time during the α + β3b deactivation tails supports the view that channels must occupy different sets of open states during the deactivation process. This change in occupancy of open states would also be expected to occur during current activation as channels sequentially progress from O to O*. To confirm this expectation, instantaneous I-V curves were generated at different times after a depolarizing activation step to +160 mV (Fig. 12). At the shortest activation steps, some outward rectification was observable. As the activation step duration was increased, the instantaneous I-V was increasingly inward rectifying. These results again require a blocking model in which channels occupy at least two kinds of open states, each with a distinctly different relationship to the inactivated states.

Kinetic Properties of Inactivation of α + β3b Currents

Here, we provide an empirical description of some of the kinetic properties of α + β3b currents and consider how these processes may relate to Scheme 2.

The Time Constant of Macroscopic Inactivation (τ_i). Upon depolarization from negative holding potentials with Ca^{2+} of 10 μM and higher, α + β3 currents rapidly activate and inactivate with τ_i of ~0.5–1.5 ms. Fig. 13 A plots τ_i measured as a function of voltage with 300 μM Ca^{2+}. τ_i becomes largely Ca^{2+} independent above 10 μM Ca^{2+}, and exhibits only a weak voltage dependence (Xia et al., 2000). From Scheme 2, transitions from both O_n to O^*_n and O^*_n to I_n might be expected to contribute to the observed relaxation. However, based both on the rapidity of instantaneous unblocking during repolarization and reblock during a subsequent depolarization, this implies that both k_b and k_u are very fast relative to k_f and k_r. This argument is, in fact, the basis for the analysis of the curvature in the instantaneous I-V curve (Figs. 8 and 9). Because of the rapidity of k_b and k_u, a channel that enters O^*_n may enter and exit states (I_n) many times before returning to O_n. Therefore, this would suggest that the macroscopic inactivation time constant, $\tau_i(V)$, would involve an apparent unblocking rate, $k_r'(V)$, defined by:

$$\tau_i(V) = 1/(k_f(V) + k_r'(V)),$$

where (4)

$$k_r' = k_r(k_u/(k_b + k_u)) = k_r \cdot 1/(1 + K_2(V)).$$

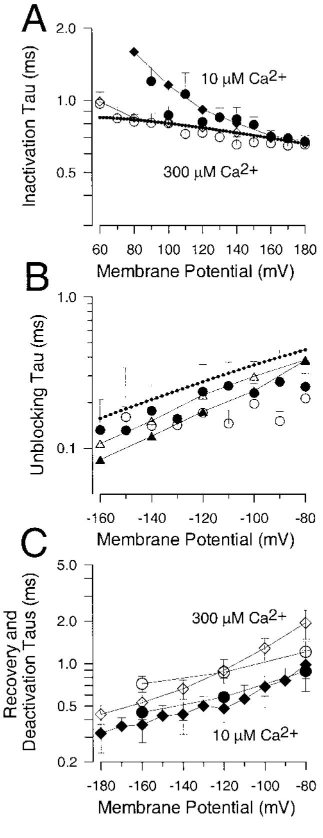

Figure 13. Kinetic characterization of α + β3b currents. In A, inactivation time constants (τ_i) were measured over a range of voltages for currents activated with either 10 (●) or 300 μM (○) Ca^{2+}. Each point represents values for 11–14 patches with error bars showing the standard deviation. Diamonds indicate τ_i measured from the simulated currents (see *Supplemental Materials*, Figure S3 available at http://www.jgp.org/cgi/content/full/117/6/583/DC1) for 10 μM (◆) and 300 μM (◇) Ca^{2+}. The dotted line was calculated from Eq. 6 with values from Table I. In B, the fast unblocking component observed in tail currents was measured from fits of $A1 \cdot \exp(-t/\tau_1) + A2 \cdot \exp(-t/\tau_2) + B$ to the α + β3b tail currents as in Figs. 5 and 7. The fast unblocking time constants plotted here were from measurements made at either 10 μM (●) and 300 (○) μM Ca^{2+} (error bars are the standard deviation). The dotted line corresponds to the expectations for the fast unblocking time constant from values in Table I assuming that Eq. 4 describes τ_u. Triangles are fitted τ_u values from simulated currents (see Fig. 15) for 10 μM (△) and 300 μM (▲) Ca^{2+}. In C, time constants for recovery in outward current amplitude measured from the paired pulse protocol of Fig. 10 are plotted as a function of recovery potential for 10 μM (●, five patches) and 300 μM (○: three patches) Ca^{2+}. For comparison, values for current deactivation of α + β3b currents at 10; ◆, seven patches) and 300 μM Ca^{2+} (◇, six patches) are also shown. Error bars indicate SD. The similarity of deactivation time constants and the recovery in amplitude from the paired pulse protocol suggests that similar rate-limiting transitions are involved for each.

Recovery from Inactivation. A number of macroscopic relaxations are observed with the recovery protocol in Fig. 10. Specifically, over some potentials, an unblocking relaxation (τ_u) was observable in the tail current, whereas relaxations could also be measured in the time constant of recovery (τ_r) of current activated at +160 mV using a paired pulse protocol. τ_u was difficult to measure reliably, but exhibited a slight voltage dependence with values in the range of 100–250 μs, being faster at more negative potentials (Fig. 13 B). No substantial difference in τ_u was observed between tail currents recorded with 10 or 300 μM Ca^{2+}, although the scatter in the estimates makes this point uncertain. Because multiple relaxations are observed in association with the recovery protocols, at negative potentials, it is tenuous to associate particular time constants with specific postulated molecular steps. However, τ_u, the unblocking relaxation, is about an order of magnitude more rapid than either the paired pulse recovery relaxation or the tail current deactivation time constant. Thus, in accordance with Scheme 2, we propose that the unblocking relaxation would primarily correspond to movement of channels from O^*_n to O_n, presumably also reflecting $1/(k_f(V) + k_r'(V))$. However, the unblocking relaxation might also reflect other kinetic processes if, for example, substantial reopening of channels may occur at particular [Ca^{2+}] or in the case that channels in preinactivated states (O^*_n) may directly deactivate.

τ_r was measured from the paired-pulse protocol for 10 and 300 μM at three different potentials (Fig. 13 C).

These values, in the range of 0.75–1.5 ms, are of the same order as τ_i measured at more positive potentials, but are also essentially identical to the time constants of deactivation (τ_d) measured from the tail current. What is the significance of τ_r? There is some suggestion that the underlying recovery process is actually better described by a two exponential time course (Fig. 10, E and F), but the two components are difficult to discern with the methods used here. However, the general correspondence of the τ_r to τ_d would argue that return of channels to states C_n is the primary determinant of the recovery in current amplitude.

Steady-state Properties of Currents Predicted by Scheme 2

The results of three separate types of protocols (Figs. 4 and 5, Fig. 10, and Figs. 11 and 12) exhibit features qualitatively consistent with Scheme 2, but inconsistent with Scheme 1. Here, we examine predictions for macroscopic G-V curves expected for either scheme. Critical to the evaluation of an inactivation model is the selection of an appropriate model for current activation. We are certainly aware of the complexities of the activation behavior of BK channel gating particularly under conditions of low or high Ca^{2+} (McManus and Magleby, 1988; Cox et al., 1997; Cui et al., 1997; Horrigan and Aldrich, 1999; Rothberg and Magleby, 1999). However, over a wide range of Ca^{2+} concentrations, the equilibria between closed and open states follows a simple behavior approximated by the voltage-dependent MWC gating model (Cox et al., 1997). Thus, here we use a 10-state MWC activation model in conjunction with the generalized blocking models of Schemes 1 and 2. The general 10-state MWC activation model (Cox et al., 1997) when expanded in accordance with Scheme 2 is given by:

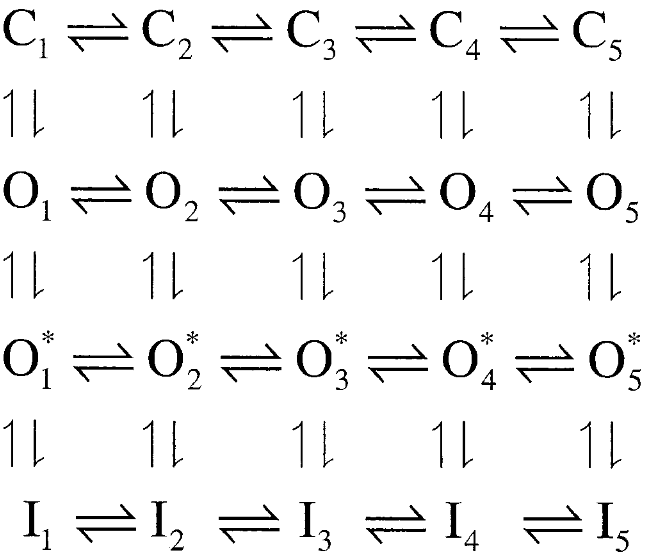

(SCHEME 2a)

where each horizontal row corresponds to Ca^{2+} association steps. If we assume that rates of entry and exit into O^*_n and I_n are identical for O_1–O_5, the following relationships are defined, with Q_1 and Q_2 representing net charge movement associated with particular reaction steps, and K_1 and K_2 representing equilibrium constants:

$$\begin{aligned} O^*/O &= K_1(V) = k_f(V)/k_r(V) \\ &= K_1(0)\cdot\exp(Q_1FV/RT),\text{ and} \\ I/O^* &= K_1(V) = k_b(V)/k_u(V) \\ &= K_2(0)\cdot\exp(Q_2FV/RT) \end{aligned}$$

Assuming that, at any command voltage, steady-state current arises from occupancy in states O_n and O^*_n, the fractional conductance is given by:

$$G_{ss}(V) = (O_n + O^*_n)/(C_n + O_n + O^*_n + I_n).$$

With $O/C = K_0(V)$,

$$\begin{aligned} G_{ss}(V) = {} & K_0(V) + K_0(V)\cdot K_1(V)/(1 + K_0(V) + \\ & K_0(V)\cdot K_1(V) + K_0(V)\cdot K_1(V)\cdot K_2(V)) \end{aligned}$$

or

$$\begin{aligned} G_{ss}(V) = {} & (1 + K_1(V))/(1 + 1/K_0(V) + K_1(V) \\ & K_0(V)\cdot K_2(V)). \end{aligned}$$

We further assume that Ca^{2+} binding among O_n^* and among I_n is identical to the Ca^{2+} association and dissociation steps among O_n. From this, the steady-state conductance arising from Scheme 2 following from Cox et al. (1997) is given by:

$$\begin{aligned} G_{ss}(V) = {} & (1 + K_1(V))/(1 + B\cdot L(0)\cdot\exp(-QFV/RT) + \\ & K_1(V) + K_1(V)\cdot K_2(V)), \end{aligned} \tag{5}$$

where B, L(0), and Q are as defined for Eq. 2 in MATERIALS AND METHODS.

For tail currents, we assume that, because of rapid unblocking during repolarization, all channels in I_n immediately return to O*. As shown experimentally, this does not appear to be the case, i.e., repolarization results in a new voltage-dependent equilibrium between O^*_n and I_n. However, at very negative repolarization potentials this simplifying assumption is not unreasonable. The peak tail currents will therefore reflect occupancy in states O, O*, and I immediately before the repolarizing voltage-step. Thus,

$$G_t(V) = (O_n + O^*_n + I_n)/(C_n + O_n + O^*_n + I_n,)$$

$$G_t(V) = (K_0(V) + K_0(V)\cdot K_1(V) + K_0(V)\cdot K_1(V)\cdot K_2(V))/(1 + K_0(V) + K_0(V)\cdot K_1(V) + K_0(V)\cdot K_1(V)\cdot K_2(V))$$

or

$$G_t(V) = (1 + K_1(V) + K_1(V)\cdot K_2(V))/(1 + B\cdot L(0)\cdot \exp(-QFV/RT) + K_1(V) + K_1(V)\cdot K_2(V)) \quad (6)$$

Similar equations, except lacking the term for $K_2(V)$, can be generated to describe the behavior of currents arising from an expanded version of Scheme 1 (15 states). Given the empirical requirement that unblocking from inactivated states is exceedingly rapid, here we consider only the case where channels blocked in accordance with Scheme 1 reopen very rapidly after repolarization, such that channels in both O and I contribute to the tail currents. More detailed evaluation of the discriminatory capability of Scheme 1 and Scheme 2 is presented in the *Online Supplemental Materials* (available at http://www.jgp.org/cgi/content/full/117/6/583/DC1).In short, this evaluation shows that families of G-V curves are unlikely to prove of much use in discerning between the two types of blocking models. However, there are two interesting facets of G-V curves predicted by either Scheme. Because of rapid unblocking and the contribution of inactivated channels to the tail currents, the $V_{0.5}$ for G-V curves measured from tail currents exhibits a pronounced leftward shift at lower Ca^{2+} relative to channels activated in the absence of inactivation. This shift in the $V_{0.5}$ is also accompanied by a steeper voltage dependence of the G-V curve.

Both the β1 and β2 subunits produce profound shifts in the curves for activation of conductance as a function of voltage at a given Ca^{2+} (McManus et al., 1995; Wallner et al., 1995, 1999; Xia et al., 1999). For non inactivating currents, such curves are typically determined from tail current measurements, whereas for inactivating currents, determination of the G-V curves for activation can be more complicated. We have previously reported that the β3b subunit produces shifts in the $V_{0.5}$ for activation at lower $[Ca^{2+}]$ than is typically observed for other β subunits (Xia et al., 2000). Our analysis here indicates that, irrespective of whether blockade occurs by either Scheme 1 or Scheme 2, a rapid blocking and unblocking process can result in an apparent shift in the $V_{0.5}$ for activation at low Ca^{2+}. Thus, the observed shift in $V_{0.5}$ seen with the β3b subunit at low Ca^{2+} (Xia et al., 2000) is consistent with a fast unblocking mechanism, but does not by itself distinguish between Scheme 1 or Scheme 2.

To define parameters for Scheme 2 that might be consistent with our results, families of G-V curves obtained from α + β3b currents were fit to either Scheme 1 or Scheme 2. Fig. 14 displays normalized tail current and steady-state current G-V curves for α + β3b currents from one patch measured with 0, 0.5, 1, 4, 10, and 300 μM Ca^{2+}. In A1 and A2, conductance values were fit with Eqs. 5 and 6 derived from Scheme 2, whereas, in B1 and B2, values were fit with similar equations derived from the expanded 15-state version of Scheme 1. Not unexpectedly, neither model clearly fits the data set better than the other. In both cases, the approximate spacing of the G-V curves is faithfully described. For either scheme, the shape of the steady-state G-V curves is reasonably well-described from 4 μM Ca^{2+} and higher. However, in both cases, the experimentally measured steady-state conductance at the most positive voltages, particularly at 0 Ca^{2+}, underestimates that expected for these models (see Fig. 1). This is observed, even though the maximal tail current conductance is similar at either 0 Ca^{2+} or 300 μM Ca^{2+}. This observation was consistently observed in all patches.

The greater reduction in steady-state current at 0 Ca^{2+} than at higher Ca^{2+} is rather unusual and was

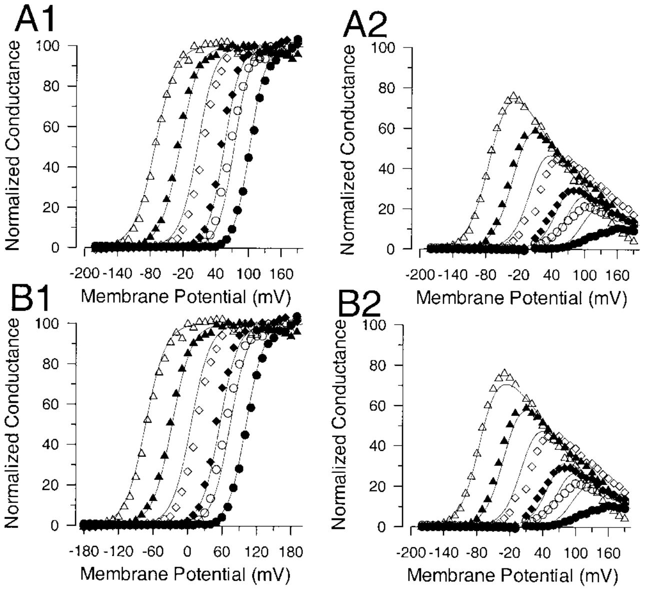

Figure 14. Families of G-V curves obtained from both steady-state and tail current measurements do not distinguish between Schemes 1 and 2. Tail current amplitudes and steady-state current amplitudes were measured in one patch at 0, 0.5, 1, 4, 10, and 300 μM Ca^{2+}. The normalized conductance is plotted as a function of command potential with tail current measurements in the left column (A1 and B1) and steady-state current estimates (A2 and B2) on the right. In A, both panels were fit simultaneously with the expanded MWC version of Scheme 2 defined by Eqs. 5 and 6. KC = 10.11 ± 0.75; K0 = 0.66 ± 0.05; L(0) = 1775.74 ± 1280; Q = 1.26e ± 0.13; $K_1(0)$ = 0.31 ± 0.10; Q_1 = 0.44e ± 0.14e; $K_2(0)$ = 2.17 ± 3.6; Q_2 = 0.19e ± 0.21. In B, both panels were fit simultaneously with similar equations defined by Scheme 1, assuming essentially instantaneous recovery from I to O at the tail current potential. KC = 11.20 ± 0.17; K0 = 0.75 ± 0.04; L(0) = 1096.3 ± 243; Q = 1.41e ± 0.045; $K_1(0)$ = 0.71 ± 0.14; Q1 = 0.342e ± 0.04.

noted previously (Xia et al., 2000). This observation would require that, at saturating activation, the equilibrium among channels in O_n, O^*_n, and I_n would differ at low and high Ca^{2+}, with greater relative occupancy of I_n at lower Ca^{2+}. This would require models in which inactivation from different states O_n is not identical. One of the limitations of the voltage-dependent MWC gating model is that it fails to account for the multiple closed and open states observed for activation of BK channels at 0 Ca^{2+} (Horrigan and Aldrich, 1999; Horrigan et al., 1999; Nimigean and Magleby, 2000; Talukder and Aldrich, 2000). In such cases, activation at 0 Ca^{2+} is presumably driven exclusively by movement of voltage sensors in each subunit, whereas, at high Ca^{2+}, Ca^{2+}-binding steps become important. Thus, to account for both the voltage-dependent and Ca^{2+}-dependent properties of the channel, two-tiered activation models for BK channels have been proposed (Rothberg and Magleby, 1999; Cox and Aldrich, 2000). Future analysis will have to consider whether inactivation might proceed somewhat differently from open states occupied at low Ca^{2+} relative to those at high Ca^{2+}. We also considered that the reduction in steady-state currents in 0 Ca^{2+} might arise from a Ca^{2+}-dependent inhibition of the blocking process. However, such a scheme would require that Ca^{2+}-dependent inhibition be saturable by ~1 μM Ca^{2+} and could not result from simple mass-action competition between Ca^{2+} and the inactivation mechanism.

TABLE I

Parameters Used for Current Simulations

Activation parameter	Range defined in Cox et al.*	Values used for current simulations	
L(0)	1,647–2,029	2,000	
Q	1.35–1.40e		
KC	8.68–11.0		
KO	1.04–1.1		
$C0 \rightarrow O0$	1.8–2.39	2	
$C1 \rightarrow O2$	5.0–7.0	6	
$C2 \rightarrow O2$	29–40	40	
$C3 \rightarrow O3$	130–295	250	
$C4 \rightarrow O4$	300	500	
q_o	0.71–0.73e	0.72e	
$O0 \rightarrow C0$	3,612–3,936	4,000	
$O1 \rightarrow C1$	1,076–1,338	1,200	
$O2 \rightarrow C2$	659–974	800	
$O3 \rightarrow C3$	486–490	500	
$O4 \rightarrow C4$	92–126	100	
q_c	−0.64 to −0.67e	−0.67e	
Ca^{2+} on rates per site	$10^9\ M^{-1}\ s^{-1}$	$10^9\ M^{-1}\ s^{-1}$	
Ca^{2+} off rates from C_n per binding site	10^9 KC	10^9 KC	
Ca^{2+} off rates from O_n per binding site	10^9 KO	10^9 KO	
Blocking parameters		$k_x(V) = k_x(0) \cdot \exp(z_xFV/RT)$	
		$k_x(0)$	z_x
$k_f(V)$ $O_n \rightarrow O^*_n$		900	0.072
$k_r(V)$ $O^*_n \rightarrow O_n$		750	0.361
$k_b(V)$ $O^*_n \rightarrow O_n$		90,000	0.084
$k_u(V)$ $I_n \rightarrow O^*_n$		80,000	0.14
Equilibrium blocking parameters		Kx(0)	net Q
$K_1(V)$		1.2	0.433e
$K_2(V)$		1.12	0.225e

Equilibrium blocking parameters are defined by $K_1(V) = k_f(V)/k_r(V) = K_1(0) \cdot \exp(-z_1FV/RT)$ and $K_2(V) = k_b(V)/k_u(V) = K_2(0) \cdot \exp(-z_2FV/RT)$.

*(Cox et al., 1997)

Scheme 2 Predicts the Unusual Behavior of the $\alpha + \beta 3b$ Currents

To test whether Scheme 2 can reproduce the key features of the $\alpha+\beta 3b$ currents, we have used estimates for activation rates for the MWC model taken from Table I of Cox et al. (1997). From Scheme 2, the following parameters for the kinetic steps involved in block were defined:

$k_f(0)$ and z_1, giving $k_f(V) = k_f(0) \cdot \exp(z_1FV/RT)$

$k_r(0)$ and z_2, giving $k_r(V) = k_r(0) \cdot \exp(z_2FV/RT)$

$k_b(0)$ and z_3, giving $k_b(V) = k_b(0) \cdot \exp(z_3FV/RT)$ and

$k_u(0)$ and z_4, giving $k_u(V) = k_u(0) \cdot \exp(z_4FV/RT)$.

Our goal was to identify a set of rates that generally reproduces the essential features of the observed currents.

The Role of k_b and k_u. Let us consider first the properties of the rapid equilibrium between O* and I. To account for the instantaneous block and unblock, k_b and k_u must be sufficiently fast that there is no detectable relaxation, at least under normal recording conditions. Thus, the actual rates of k_b and k_u are arbitrary based on the information available to us, and were chosen so that, except at infinite bandwidth, relaxations between O* and I would not be observable. The relative voltage dependence of the two rates and the ratio of the rates at positive potentials are very critical in terms of defining the steady-state levels of current at the positive potentials. Empirically, it is observed that outward current levels at different voltages tend to remain constant over a range of positive voltages (as seen in the actual data records of Fig. 1). This required values for the net charge associated with the O* to I equilibrium of ~0.2e–0.25e. This agrees with the value of 0.21e obtained from fitting the instantaneous I-V curve in Fig. 8.

The Role of k_f and k_r. Several factors dictate appropriate choices of values for k_f and k_r. First, given the mild voltage dependence of τ_i, the voltage dependence of k_f must be relatively weak. Second, if k_r is too slow, it re-

TABLE II

Equilibrium Parameters for Activation and Inactivation

Activation parameter	Range defined in Cox et al.[*]		Values from fit to G-V curves			
L(0)	1,647–2,029		1,775 ± 1,280			
Q	1.35–1.40e		1.26 ± 0.13e			
KC	8.68–11.0		10.11 ± 0.75			
KO	1.04–1.1		0.66 ± 0.005			
Equilibrium inactivation parameters	Values used for simulating currents		Values obtained from fit to G-V curves[‡]		Values obtained from fit to instantaneous I-V[§]	
Blocking parameters: $Kx(V) = K_x(0) \cdot \exp(Q_xFV/RT)$	$K_x(0)$	Q_x	$K_x(0)$	Q_x	$K_x(0)$	Q_x
$K_1(V)$	1.2	0.433e	0.31 ± 0.1	0.44e ± 0.014		
$K_2(V)$	1.12	0.225e	2.17 ± 3.6	0.19e ± 0.2	2.27 ± 0.045	0.21e ± 0.005

[*] (Cox et al., 1997).

[‡] (Fig. 14).

[§] (Fig. 8).

sults in an excessive slowing of tail currents. However, if k_r is too fast and has appreciable voltage dependence, it will contribute to a voltage dependence of τ_i that is inconsistent with the results. The precise value of k_r and its voltage dependence seem to be parameters that are most critical in trying to account for several aspects of the data. From these considerations, transition rates between O and O* were adjusted to result in values for the macroscopic τ_i and τ_d that approximate those seen experimentally. In our adjustment of parameters, we also took into account estimates for equilibrium values for $K_1(0)$, Q_1, $K_2(0)$, and Q_2 made from fits of the macroscopic tail and steady-state G-V curves in Fig. 14 and for estimates of $K_2(0)$ and Q_2 from fits to the instantaneous I-V curves in Figs. 8 and 9.

Based on the above, a set of values were chosen that reasonably reproduced the kinetic properties of the blocking and unblocking relaxations observed in the raw currents we have examined. Table II provides a listing of the values for the parameters used in the simulations and also those obtained from the two fitting procedures. In general, there is reasonable agreement among all values except for $K_1(0)$. Of all equilibrium values, that for Q_2 is probably the most accurately constrained, since it is this value that primarily defines the slope of the steady-state G-V curves at positive voltages.

Effects of Short and Longer Activation Steps on Tail Current Properties. Currents were simulated with a stimulation protocol similar to that used to activate currents in Fig. 2. Assuming 10 μM Ca^{2+}, tail currents were elicited at either −80 (Fig. 15, A1) or −160 mV (Fig. 15, A2) after either a 1- or 10-ms step to +120 mV. For tails examined at −80 mV, the tail current amplitude was essentially identical for both 1- and 10-ms command steps, despite the fact that the outward current at 1 ms greatly exceeded the outward current at 10 ms. Furthermore, with the repolarization to −80 mV, the tail current exhibits the shoulder of unblocking observed in the α + β3b currents. For tails examined at −160 mV, the tail current after the 10-ms step actually exceeds that observed after the 1-ms step, similar to Fig. 5. Despite the unblocking shoulder in the tail current at −80 mV after the 10-ms step, single exponential functions fit to the tail currents after either 1- or 10-ms activation steps yielded similar values (see Fig. 15 legend).

Paired Pulse Recovery Properties Predicted by Scheme 2. Currents were simulated with parameters given in Table I with a stimulation protocol similar to that used in Fig. 10. Assuming 10 μM Ca^{2+}, a pair of test steps to +160 mV were separated by recovery steps to −80 mV ranging from 50 μs to 8 ms duration (Fig. 15 B). Similar to the α + β3b currents, despite the rapid recovery from inactivation seen in the tail current amplitude, there is a slower increase in peak current amplitude during the second test step as the duration of the recovery interval is increased. With the shorter recovery steps (e.g., 50 μs), a subsequent depolarization results in a nonohmic step in current which only slightly exceeds the previous steady-state level of current at +160 mV. With longer recovery steps, the second step to +160 mV evokes a more ohmic step in current. These features recapitulate those observed for the α + β3b currents. For brief recovery steps, there is a spike of current at the onset of the second step to +160 mV. This represents the ohmic current through channels in states O* that become blocked within 20 μs during the step to +160 mV and would not be detected with typical recording conditions.

Scheme 2 Predicts Changes in the Instantaneous I-V Curves. Instantaneous I-V curves were simulated with a protocol similar to that used in Fig. 11. After activation of current at +160 mV with 10 μM Ca^{2+}, a repolarization to −120 mV of either 100- or 500-μs duration preceded a subsequent step to potentials between −120

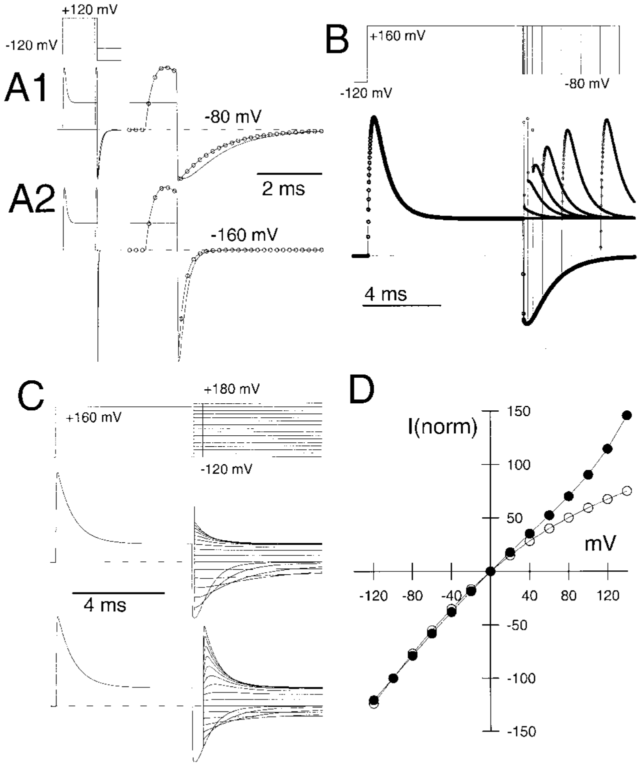

FIGURE 15. Scheme 2 predicts currents that exhibit properties similar to those observed for α + β3b currents. In A, Scheme 2 (with parameters in Table I), assuming 10 μM Ca^{2+}, was used to simulate currents with the indicated protocol (as in Fig. 2). Tail currents were compared at either −80 mV (A1) or −160 mV (A2), after either a short (1 ms) or longer (10 ms) activation step. Single exponential fits to the decay phases yielded time constants of 1.23 and 1.24 ms, for the shorter and longer activation steps, respectively. In A2, tail current was elicited at −160 mV. Time constants of deactivation were 0.227 ms (longer step) and 0.221 ms. In B, a paired-pulse protocol (as in Fig. 10) was used to model the recovery from inactivation with Scheme 2 (values from Table I; 10 μM Ca^{2+}). Points show each simulated value (10 μs). The tail current exhibits the rapid nonohmic unblocking, followed by a slower unblocking. After the shorter recovery steps (500 μs), a subsequent depolarization to +160 mV results in rapid reblock with only a small excess of current over the previous steady-state level of block. Longer recovery steps result in an increase in the initial amount of current observed during the step to +160 mV, even as the tail current at −80 mV decreases. For the transition rates between O* and I in Table I, at short recovery times the step to +160 mV also results in a 10–20-μs rapid spike of current associated with the rapid reblocking of channels from O* to I. Currents were simulated at 10 μs per point, and the spike of current lasted 1–2 points. In C, the indicated protocol (as in Fig. 11) was used to simulate currents assuming 10 μM Ca^{2+}. In the middle panel, a 100-μs recovery step to −120 mV preceded a subsequent step to potentials between −120 and +180 mV. In the bottom panel, a 500-μs step to −120 mV was used to produce recovery from inactivation. In D, the instantaneous I-V from the traces in C were determined by measuring current values 30 μs after the nominal end of the recovery steps. Values were normalized to current amplitudes at −100 mV. At 30 μs, the spike of reblocking observed in the simulated currents is complete. The I-V curve becomes more linear after the 500-μs recovery step (●), which is indicative of greater occupancy of O_n. Simulation frequency: 100 kHz.

mV and +180 mV (Fig. 15 C). Instantaneous I-V curves were generated by measurement of the current amplitude 30 μs after the time of the activation step (Fig. 15 D). At this time point, the initial spike of current is complete, but any secondary activation of closed channels has scarcely begun. Current measured following the 100 μs recovery step to −120 mV exhibits the inward rectification typical of the α + β3b currents. With the longer 500-μs recovery step, the I-V curve has changed, becoming more linear. The slight upward curvature seen at the most positive potentials represents the slight activation of channels closed at the onset of the voltage-step. Thus, Scheme 2 is sufficient to predict changes in the instantaneous I-V curves similar to those seen with the α + β3b currents.

The predictions of Scheme 2 (from the values in Table I) for the instantaneous I-V curve and the behavior of τ_i and τ_u as a function of voltage are overlaid over the actual data points in Fig. 9 A and Fig. 13, A and B, respectively.

DISCUSSION

Rapid inactivation of voltage-dependent K^+ channels mediated by NH_2-terminal domains, either of the pore-forming α subunits (Hoshi et al., 1990; Ruppersberg et al., 1991; Tseng-Crank et al., 1993) or of auxiliary β subunits (Rettig et al., 1994; Morales et al., 1995; Rasmusson et al., 1997), has typically been analyzed with a simple scheme in which binding of the inactivation domain to a binding site directly results in cessation of ion permeation (Hoshi et al., 1990; Demo and Yellen, 1991; MacKinnon et al., 1993). Kinetic features of inactivation onset and recovery support the idea that a single molecular step governs the blocking process. While in its inactivating position, the inactivation domain is thought to rest in intimate association with the mouth of the ion permeation pathway. This assertion is based on multiple types of evidence. Cytosolic blockers impede the movement of the inactivation domain to its blocking site (Choi et al., 1991). Occupancy of the ion permeation pathway by permeant ions favors dissociation of the inactivation domain from its binding site (Gomez-Lagunas and Armstrong, 1994). After repolarization, occupancy of its binding site by the inactivation domain inhibits movement of the open pore to a closed conformation resulting in channel reopening during recovery from inactivation (Demo and Yellen, 1991; Ruppersberg et al., 1991). Furthermore, residues in the S4-S5 loop are thought to contribute to the inactivation domain binding site and also influence ion permeation (Isacoff et al., 1991).

Inactivation mediated by NH_2 termini of BK β subunits (Wallner et al., 1999; Xia et al., 1999; Xia et al., 2000) shares with *Shaker*B inactivation (MacKinnon et al., 1993; Gomez-Lagunas and Armstrong, 1995) the fact that each of the up to four inactivation domains per channel appears to function independently to produce inactivation (Ding et al., 1998). However, unlike voltage-dependent K^+ channel inactivation, cytosolic blockers do not impede the BK inactivation process (Solaro et al., 1997; Xia et al., 1999, 2000) and channels can recover from the inactivated state without passing through open states (Solaro et al., 1997). These results have suggested that the NH_2 terminus of the β2 subunit may not directly occlude the mouth of the channel, although binding at a more superficial site might account for the blocking effect.

Inactivation mediated by the β3b subunit also exhibits features inconsistent with the simple occlusion model proposed for ball-and-chain inactivation mechanisms. First, inactivated channels exhibit two unblocking components after repolarization: an essentially nonohmic, instantaneous increase in tail current, followed by a small secondary time-dependent unblock. Second, after short repolarizations that drive inactivated channels back to open states, a subsequent depolarization will result in an essentially instantaneous reblock of those open channels, despite the slower inactivation kinetics observed when channels are activated from closed states. Third, instantaneous I-V curves generated at different times during deactivation indicate that channels occupy multiple kinds of open states.

To account for our observations, we proposed an extension to the simple, open channel block model, namely that a transition to a preinactivated open state precedes a subsequent blocking step. This model, given in Scheme 2a, reproduces most of the novel features of the α + β3b currents, including the instantaneous unblock and subsequent slower unblock in the tail currents, the characteristics of the paired pulse protocols, and the changes in the instantaneous I-V curves at different times during activation and deactivation. Although rates for Scheme 1 can be chosen to produce rapid unblocking upon repolarization, Scheme 1 is entirely unable to account for other aspects of the results. In contrast, using rates constrained by those suggested from experimental observations, it was possible to simulate currents from Scheme 2 that approximated the key kinetic and steady-state features of the α + β3 currents.

Although we have not systematically evaluated a variety of models, a number of factors suggest that Scheme 2 provides the simplest extension of Scheme 1 that can account for most of our results. As argued, at least two kinetic states must contribute to the blocking reaction. Furthermore, among other factors, the changes in the shape of the instantaneous I-V curve argue quite compellingly for the existence of a type of open state distinct from those that occur when the NH_2 terminus is absent. This behavior of the instantaneous I-V curves, therefore, excludes models with a single category of open state but with multiple closed, inactivated states such as ($O \rightleftharpoons I_1 \rightleftharpoons I_2$). It might also be argued that the inactivated state represents an open state with less than a full-conductance, such that the blocking scheme would be $O \rightleftharpoons O_s$, where O_s has a conductance that is a small fraction of that of O. Such a model could approximate our results if the single-channel conductance of O_s were markedly voltage-dependent. Such a model is, in essence, functionally equivalent to that given in Scheme 2, in that a voltage-dependent single-channel conductance approximates the rapid two-state transitions between O* and I. We prefer Scheme 2, however, since it provides an explicit kinetic step to account for the apparent voltage dependence of conductance.

The inward rectification resulting from the rapid block and unblock of open α + β3b channels is somewhat reminiscent of cytosolic blockade of BK channels produced by two peptides, bovine pancreatic trypsin inhibitor (BPTI) and dendrotoxin (DTX; Lucchesi and Moczydlowski, 1991; Moss and Moczydlowski, 1996; Favre and Moczydlowski, 1999). Blockade by these peptides is associated with the appearance of subconductance states that arise from rapid flickering between open and closed states (Moss and Moczydlowski, 1996). The subconductance states exhibit inwardly rectifying behavior, presumably because of the voltage dependence of the processes controlling opening and closing during the rapid flickering (Moss and Moczydlowski, 1996). These results have been interpreted in terms of a fluctuating barrier within the ion permeation pathway that is allosterically regulated by binding of BPTI or DTX to sites outside the channel pore. Analysis of blockade by Ba^{2+} in the presence and absence of BPTI has supported the idea that binding of Ba^{2+} to the channel is unaffected whether BPTI is bound or not (Lucchesi and Moczydlowski, 1991). Thus, BPTI and DTX appear to bind to sites that do not prevent access by Ba^{2+} (or TEA) to the cytosolic mouth of the channel. Similarly, TEA does not inhibit access of the α + β3b inactivation domain to the inactivation site. Thus, it is possible that both blockade by BPTI and inactivation may involve actions at sites peripheral to the ion permeation pathway, that then promote rapid flickery opening and closing of the channel. Future work will be required to assess whether block by BPTI is related the inactivation behavior described here.

Aspects of α + β3b Currents Not Explained by the Two-Step Blocking Model

Outward Rectification in Instantaneous I-V Curves. One characteristic of α + β3b currents not considered by the proposed model is the outward rectification observed in the instantaneous I-V curves, under conditions when inactivation is abolished or not yet developed. This is particularly apparent following removal of inactivation by trypsin, and by molecular deletion of the β3b NH_2 terminus (Zeng et al., 2001). The presence of the outward rectification following removal of NH_2 and COOH termini indicates that the nonlinearity is unrelated to the inactivation mechanism we have studied and we expect that it will occur in parallel with any ongoing inactivation mechanism. Because of this nonlinearity in the instantaneous I-V curve, the shape of the steady-state and peak G-V curves arising from the α + β3b currents and also the instantaneous I-V curves with inactivation intact will be biased by this secondary effect. However, this phenomenon will have essentially no effect on any of the basic conclusions we have drawn that depend on the kinetic characteristics of the β3b inactivation mechanism.

Smaller Steady-state Currents at Lower Ca^{2+}. Another unexplained aspect of α + β3b currents is that, at positive potentials with zero or very low Ca^{2+}, the steady-state currents are smaller than would be expected based on the size of the tail currents (Fig. 1). The similarity of peak tail current after activation to very positive potentials at both 0 Ca^{2+} and 300 μM Ca^{2+} would suggest that, in accordance with any rapid blocking scheme, the same fraction of channels occupy activated states (e.g., O_n, O^*_n, and I_n) at both low and high Ca^{2+}. For the steady-state level of current to be less at lower Ca^{2+} would require that the distribution of channels among the activated states favor I_n at lower Ca^{2+}. This condition cannot be achieved by any kind of model in which inactivation from all open states is identical. However, if the affinity of the inactivation domain to channels that are activated primarily as a consequence of voltage sensor movement was stronger than to channels activated primarily as a consequence of Ca^{2+}-dependent transitions, it might be possible to account for this behavior. An extension of the 50-state two-tiered model (Horrigan and Aldrich, 1999; Rothberg and Magleby, 1999; Cox and Aldrich, 2000) to include inactivation might help address this possibility.

Lack of Contribution of Recovery from Inactivation to Tail Current Deactivation. Both the linear blocking models of Schemes 1 and 2 suggest that, during repolarization, when recovery from inactivation is not complete, the kinetics of blocking transitions should contribute to the tail current relaxation time course. However, two observations have indicated that the kinetics of the blocking reactions do not contribute to the final exponential decay of the deactivation time course. First, τ_d was similar for constructs either with or without the inactivating NH_2 terminus. Second, τ_d was similar before and after removal of inactivation by trypsin. Both observations are obviously inconsistent with either Scheme 1 or Scheme 2. We envision two possible explanations for this lack of participation of blocking reactions in the deactivation time course. In one case, the rates of return of channels to states (O_n) may be sufficiently fast compared with the closing rates that deactivation time constants are unaffected by the blocking steps. This explanation seems unlikely, since there should then be little difference in peak tail current amplitude before and after trypsin application. On the other hand, the lack of influence of inactivation on deactivation kinetics could also arise, if there were pathways by which channels in inactivation-specific states (O^*_n and I_n) could return to closed pathways without returning through O_n. A model of this kind is given in Scheme 3:

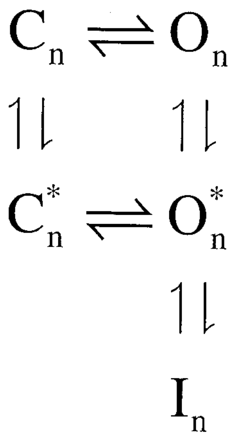

(SCHEME 3)

In this model, occupancy of channels in states I_n and O^*_n does not impede their return to closed states. This modification to Scheme 2, with appropriate rates, can still qualitatively reproduce the key features of the α + β3b currents, but does a better job of accounting for the properties of τ_d. In addition to explaining the lack of change in τ_d after the removal of the NH_2 terminus, Scheme 3 may help account for the large increase in outward current after trypsin-mediated removal of inactivation. The enormous increase in the peak currents after trypsin application suggests that, with the inactivation mechanism intact, there may be more entry into inactivated states from closed states than would be predicted by linear blocking models. The moderate increase in tail current amplitudes after trypsin application indicates that a similar number of channels are activated in both cases. However, the discrepancy between peak current values before and after trypsin indicates that many channels that contribute to the tail current before trypsin are contributing less than expected to the outward current, raising the possibility of entry into inactivated states from closed states.

In sum, the results have indicated that Scheme 2 accounts for many unusual features of the α + β3b behaviors, although some aspects of the α + β3b currents remain unexplained. From considerations just given, a relatively simple modification to Scheme 2 may resolve some of the unexplained features of the data, and this will have to be evaluated in the future. We have chosen to focus on Scheme 2, since it represents a simple, one step extension of the standard, simple-block scheme and accounts for the key features of block over most conditions. The ability of Scheme 2 to account for so many aspects of the $\alpha + \beta 3b$ currents indicates that it can serve as a suitable working hypothesis for further exploration of the mechanism and structural basis for inactivation of BK channels by auxiliary subunits.

What Is the Physical Basis for the Two-Step Inactivation Process?

A kinetic model, although perhaps describing the behavior of a current, does not define a plausible physical picture of the underlying mechanism. The two-step blocking model allows two quite distinct types of physical interpretations. In one case, the two separate steps in Scheme 2 would represent, first, a binding of an inactivation domain to a nonblocking position on the α (or portions of the β3b) subunit and, second, movement of that tethered NH_2-terminal domain into a position that occludes the ion permeation pathway. Thus, the two-step mechanism would comprise an initial binding step, and then block. Thus, in contrast to the simple block model, the binding of the NH_2 terminus would not directly result in block of ion permeation. With this view, the blocking step could also represent an allosteric closing of the channel. A second view would be that the initial reaction step corresponds to some conformational movement in the open channel complex that then allows the rapid binding and unbinding of the NH_2 terminus to a blocking site. However, irrespective of the mechanism of the actual block of the channel, energetically it must represent formation of a nonconducting state that is distinct from the normal closed conformation of the channel.

The β2 subunit also confers inactivation on BK channels (Wallner et al., 1999; Xia et al., 1999). Inactivation mediated by β2 is substantially slower than that mediated by β3b and the steady-state level of β2 inactivation is much more complete than for the β3b subunit. However, in both cases, cytosolic blockers do not slow either inactivation process. Furthermore, in both cases, it appears that channels can return to closed states directly from inactivated states (or preinactivated states), i.e., reopening is not necessary for channels to return to resting states. This behavior, which differs from the situation for *Shaker* K^+ channel inactivation, suggests that the two mechanisms are somehow similar and raise the possibility that the apparent differences between β subunits may only arise because of the particular rates and voltage dependencies of the particular transitions between $(O \rightleftharpoons O^* \rightleftharpoons I)$. In fact, it is a relatively simple matter to adjust the rates in Scheme 2 to obtain currents which qualitatively resemble those obtained with $\alpha + \beta 2$ coexpression. Future work in conjunction with mutational analysis of the β2 and β3b NH_2 termini may allow molecular dissection of the elements necessary for the inactivation process and a separation of factors that may contribute to the binding and blocking steps.

We thank Anne Benz and the C. Zorumski laboratory for providing us with oocytes, Lynn Lavack for assistance with injection and maintenance of oocytes, and Joe Henry Steinbach for comments on early versions of this manuscript.

This work was supported by the National Institutes of Health grant DK46564 (to C. Lingle).

Received: 1 February 2001
Revised: 19 February 2001
Accepted: 20 April 2001

REFERENCES

Bezanilla, F., and C.M. Armstrong. 1977. Inactivation of the sodium channel. I. Sodium current experiments. *J. Gen. Physiol.* 70:549–566.

Choi, K.L., R.W. Aldrich, and G. Yellen. 1991. Tetraethylammonium blockade distinguishes two inactivation mechanisms in voltage-activated K^+ channels. *Proc. Natl. Acad. Sci. USA.* 88:5092–5095.

Cox, D., and R. Aldrich. 2000. Role of the β1 subunit in large-conductance Ca^{2+}-activated K^+ channel gating energetics. Mechanisms of enhanced Ca^{2+} sensitivity. *J. Gen. Physiol.* 116:411–432.

Cox, D.H., J. Cui, and R.W. Aldrich. 1997. Allosteric gating of a large conductance Ca-activated K^+ channel. *J. Gen. Physiol.* 110:257–281.

Cui, J., D.H. Cox, and R.W. Aldrich. 1997. Intrinsic voltage dependence and Ca2+ regulation of mslo large conductance Ca-activated K+ channels. *J. Gen. Physiol.* 109:647–673.

Demo, S.D., and G. Yellen. 1991. The inactivation gate of the *Shaker* K^+ channel behaves like an open-channel blocker. *Neuron.* 7:743–753.

Ding, J.P., Z.W. Li, and C.J. Lingle. 1998. Inactivating BK channels in rat chromaffin cells may arise from heteromultimeric assembly of distinct inactivation-competent and noninactivating subunits. *Biophys. J.* 74:268–289.

Favre, I., and E. Moczydlowski. 1999. Simultaneous binding of basic peptides at intracellular sites on a large conductance Ca^{2+}-activated K^+ channel. Equilibrium and kinetic basis of negatively coupled ligand interactions. *J. Gen. Physiol.* 113:295–320.

Gomez-Lagunas, F., and C.M. Armstrong. 1994. The relation between ion permeation and recovery from inactivation of ShakerB K^+ channels. *Biophys. J.* 67:1806–1815.

Gomez-Lagunas, F., and C.M. Armstrong. 1995. Inactivation in *Shaker*B K^+ channels: a test for the number of inactivating particles on each channel. *Biophys. J.* 68:89–95.

Hamill, O.P., A. Marty, E. Neher, B. Sakmann, and F.J. Sigworth. 1981. Improved patch-clamp techniques for high-resolution current recording from cells and cell-free membrane patches. *Pflugers Arch.* 391:85–100.

Horrigan, F.T., and R.W. Aldrich. 1999. Allosteric voltage gating of potassium channels II. Mslo channel gating charge movement in the absence of Ca^{2+}. *J. Gen. Physiol.* 114:305–336.

Horrigan, F.T., J. Cui, and R.W. Aldrich. 1999. Allosteric voltage gating of potassium channels I. Mslo ionic currents in the absence of Ca^{2+}. *J. Gen. Physiol.* 114:277–304.

Hoshi, T., W.N. Zagotta, and R.W. Aldrich. 1990. Biophysical and molecular mechanisms of *Shaker* potassium channel inactivation. *Science.* 250:533–538.

Isacoff, E.Y., Y.N. Jan, and L.Y. Jan. 1991. Putative receptor for the cytoplasmic inactivation gate in the *Shaker* K^+ channel. *Nature.* 353:86–90.

Lucchesi, K.J., and E. Moczydlowski. 1991. On the interaction of bovine pancreatic trypsin inhibitor with maxi Ca^{2+}-activated K^+ channels. A model system for analysis of peptide-induced subconductance states. *J. Gen. Physiol.* 97:1295–1319.

MacKinnon, R., R.W. Aldrich, and A.W. Lee. 1993. Functional stoichiometry of *Shaker* potassium channel inactivation. *Science.* 262: 757–759.

McManus, O.B., L.M. Helms, L. Pallanck, B. Ganetzky, R. Swanson, and R.J. Leonard. 1995. Functional role of the beta subunit of high conductance calcium-activated potassium channels. *Neuron.* 14:645–650.

McManus, O.B., and K.L. Magleby. 1988. Kinetic states and modes of single large-conductance calcium-activated potassium channels in cultured rat skeletal muscle. *J. Physiol.* 402:79–120.

Morales, M.J., R.C. Castellino, A.L. Crews, R.L. Rasmusson, and H.C. Strauss. 1995. A novel beta subunit increases rate of inactivation of specific voltage-gated potassium channel alpha subunits. *J. Biol. Chem.* 270:6272–6277.

Moss, G.W., and E. Moczydlowski. 1996. Rectifying conductance substates in a large conductance Ca^{2+}-activated K^+ channel: evidence for a fluctuating barrier mechanism. *J. Gen. Physiol.* 107:47–68.

Murrell-Lagnado, R.D., and R.W. Aldrich. 1993a. Energetics of *Shaker* K channels block by inactivation peptides. *J. Gen. Physiol.* 102:977–1003.

Murrell-Lagnado, R.D., and R.W. Aldrich. 1993b. Interactions of amino terminal domains of *Shaker* K channels with a pore blocking site studied with synthetic peptides. *J. Gen. Physiol.* 102:949–975.

Nimigean, C.M., and K.L. Magleby. 2000. Functional coupling of the $\beta(1)$ subunit to the large conductance Ca^{2+}-activated K^+ channel in the absence of Ca^{2+}. Increased Ca^{2+} sensitivity from a Ca^{2+}-independent mechanism. *J. Gen. Physiol.* 115:719–736.

Press, W.H., B.P. Flannery, S.A. Teukolsky, and W.T. Vetterling. 1989. Numerical Recipes, The Art of Scientific Computing, FORTRAN Version. Cambridge University Press, Cambridge. 702 pp.

Rasmusson, R.L., S. Wang, R.C. Castellino, M.J. Morales, and H.C. Strauss. 1997. The beta subunit, Kv beta 1.2, acts as a rapid open channel blocker of NH_2-terminal deleted Kv1.4 alpha-subunits. *Adv. Exp. Med. Biol.* 430:29–37.

Rettig, J., S.H. Heinemann, F. Wunder, C. Lorra, D.N. Parcej, J.O. Dolly, and O. Pongs. 1994. Inactivation properties of voltage-gated K^+ channels altered by presence of beta-subunit. *Nature.* 369:289–294.

Rothberg, B.S., and K.L. Magleby. 1999. Gating kinetics of single large-conductance Ca^{2+}-activated K^+ channels in high Ca^{2+} suggest a two-tiered allosteric gating mechanism. *J. Gen. Physiol.* 114: 93–124.

Ruppersberg, J.P., R. Frank, O. Pongs, and M. Stocker. 1991. Cloned neuronal IK(A) channels reopen during recovery from inactivation. *Nature.* 353:657–660.

Solaro, C.R., J.P. Ding, Z.W. Li, and C.J. Lingle. 1997. The cytosolic inactivation domains of BK_i channels in rat chromaffin cells do not behave like simple, open-channel blockers. *Biophys. J.* 73: 819–830.

Solaro, C.R., and C.J. Lingle. 1992. Trypsin-sensitive, rapid inactivation of a calcium-activated potassium channel. *Science.* 257:1694–1698.

Talukder, G., and R.W. Aldrich. 2000. Complex voltage-dependent behavior of single unliganded calcium-sensitive potassium channels. *Biophys. J.* 78:761–772.

Tseng-Crank, J., J.A. Yao, M.F. Berman, and G.N. Tseng. 1993. Functional role of the NH_2-terminal cytoplasmic domain of a mammalian A-type K channel. *J. Gen. Physiol.* 102:1057–1083.

Uebele, V., T. Wade, P. Bennett, R. Swanson, and A. Lagrutta. 2000. A novel family of alternatively spliced BK β-subunits. *Biophys. J.* 78:91. (Abstr.)

Wallner, M., P. Meera, M. Ottolia, G.J. Kaczorowski, R. Latorre, M.L. Garcia, E. Stefani, and L. Toro. 1995. Characterization of and modulation by a beta-subunit of a human maxi KCa channel cloned from myometrium. *Receptors Channels.* 3:185–199.

Wallner, M., P. Meera, and L. Toro. 1999. Molecular basis of fast inactivation in voltage and Ca^{2+}-activated K^+ channels: a transmembrane beta-subunit homolog. *Proc. Natl. Acad. Sci. USA.* 96: 4137–4142.

Xia, X.M., J.P. Ding, and C.J. Lingle. 1999. Molecular basis for the inactivation of Ca^{2+}- and voltage-dependent BK channels in adrenal chromaffin cells and rat insulinoma tumor cells. *J. Neurosci.* 19:5255–5264.

Xia, X.M., B. Fakler, A. Rivard, G. Wayman, T. Johnson-Pais, J.E. Keen, T. Ishii, B. Hirschberg, C.T. Bond, S. Lutsenko, et al. 1998. Mechanism of calcium gating in small-conductance calcium-activated potassium channels. *Nature.* 395:503–507.

Xia, X.-M., J. Ding, X.-H. Zeng, K.-L. Duan, and C. Lingle. 2000. Rectification and rapid activation at low Ca^{2+} of Ca^{2+}-activated, voltage-dependent BK currents: consequences of rapid inactivation by a novel β subunit. *J. Neurosci.* 201:4890–4903.

Zeng, X.-H., X.-M. Xia, and C.J. Lingle. 2001. Gating properties conferred on BK channels by the β3b auxiliary subunit in the absence of its NH_2 and COOH termini. *J. Gen. Physiol.* 117:607–627.